

1 **Sea-ice albedo feedback: comparison of model and observational based**  
2 **estimates**

3 Aaron Donohoe\*

4 *Applied Physics Laboratory, University of Washington, Seattle, Washington*

5 Ed Blanchard-Wrigglesworth

6 *Department of Atmospheric Sciences, University of Washington, Seattle, WA, USA*

7 Axel Schweiger

8 *Polar Science Center, Applied Physics Laboratory, University of Washington, Seattle,*  
9 *Washington, USA*

10 Philip J. Rasch

11 *Pacific Northwest National Laboratory, Richland, WA, USA*

12 \*Corresponding author address: Polar Science Center, University of Washington, Seattle, Wash-  
13 ington/USA

14 E-mail: adonohoe@u.washington.edu

## ABSTRACT

15 The sea-ice-albedo feedback (SIAF) is the product of the ice sensitivity  
16 (IS) – how much the surface albedo in sea-ice regions changes as the planet  
17 warms– and the radiative sensitivity (RS) – how much the top of atmosphere  
18 radiation changes as the surface albedo changes. We demonstrate that the RS  
19 calculated from radiative kernels in climate models is reproduced from calcu-  
20 lations using the “approximate partial radiative perturbation” method that uses  
21 the climatological radiative fluxes at the top of atmosphere and the assumption  
22 that the atmosphere is isotropic to shortwave radiation. This method facilitates  
23 the comparison of RS from satellite-based estimates of climatological radia-  
24 tive fluxes with RS estimates across a full suite of coupled climate models  
25 and, thus, allows model evaluation of a quantity important in characterizing  
26 the climate impact of sea ice concentration changes. The satellite based RS  
27 is within the model range of RS that differs by a factor of two across climate  
28 models in both the Arctic and Southern Ocean. Observed trends in Arctic sea  
29 ice are used to estimate IS which, in conjunction with the satellite-based RS  
30 yields an SIAF of  $0.16 \pm 0.04 \text{ W m}^{-2} \text{ K}^{-1}$ . This Arctic SIAF estimate sug-  
31 gests a modest amplification of future global surface temperature change by  
32 approximately 14% *relative to a climate system with no SIAF*. We calculate  
33 the global surface albedo feedback in climate models using model specific RS  
34 and IS and find a model mean feedback parameter of  $0.37 \text{ W m}^{-2} \text{ K}^{-1}$  which  
35 is 40% larger than the IPCC AR5 estimate based on using RS calculated from  
36 radiative kernel calculations in a single climate model.

## 37 1. Introduction

38 Sea ice area is expected to decrease as the climate system warms, and this in turn will lead to  
39 a darker surface, and increase in solar radiation absorbed by the climate system. This additional  
40 radiative input reinforces the initial warming providing a positive climate feedback often termed  
41 the sea-ice-albedo feedback (SIAF). Early literature on climate stability in simplified models sug-  
42 gested that SIAF could cause abrupt and dramatic climate state transitions under smoothly varying  
43 external forcing (North 1984; Budyko 1969) or produce multiple equilibria in more comprehensive  
44 coupled climate models (Ferreira et al. 2011). More modest estimates of SIAF were found in cou-  
45 pled climate models (Stocker et al. 2013; Bony et al. 2006; Soden and Held 2006a), producing an  
46 IPCC AR5 ensemble mean global SIAF of  $0.26 \text{ W m}^{-2}\text{K}^{-1}$  (Flato et al. 2013) leading to a 22%  
47 increase in the global climate response to external forcing (Roe 2009) relative to system with no  
48 SIAF. Pistone et al. (2014, 2019) used the co-variance of year-to-year sea ice anomalies and satel-  
49 lite radiation to produce an observationally based estimate of SIAF with a similar magnitude for  
50 the Arctic sea ice ( $0.31 \text{ W m}^{-2}\text{K}^{-1}$ ) and pointed out this additional radiative input to the climate  
51 system due to Arctic ice melt to date 25% the anthropogenic forcing. There is still a substantial  
52 ( $\pm 0.1 \text{ W m}^{-2}\text{K}^{-1}$ ) inter-model spread in strength of the SIAF (Yu et al. 2006; Hall and Qu 2006)  
53 that is understood to be the leading cause of inter-model differences in the high latitude climate  
54 response (polar amplification) (Hall 2004; Kay et al. 2012) (Holland and Bitz 2003).

55 SIAF measures how much additional radiative energy the Earth system gains due to sea ice  
56 loss as the planet warms, which amplifies the warming relative to a system with no SIAF. SIAF  
57 is quantified as the global (area weighted) average of  $\text{RI}_{TOA,\alpha}$ , the Radiative Impact of sea ice  
58 change (the local TOA radiative flux change due to surface albedo changes ( $\alpha$ ) from sea ice loss  
59 per degree of global averaged surface temperature change):

$$SIAF = [RI_{TOA,\alpha}(x,y)] \quad (1)$$

60 where  $[\ ]$  brackets indicate a global average. Following Yu et al. (2006, Eq. 1), the spatial map of  
 61  $RI_{TOA,\alpha}(x,y)$  is the product of two quantities (Soden and Held 2006b; Shell et al. 2008): 1.) the  
 62 surface albedo change due to sea ice loss per unit of global mean surface temperature change,  $[dT_S]$ ,  
 63  $(\frac{d\alpha_{SI}}{dT_S})$ , and 2.) the sensitivity of top of atmosphere (TOA) radiation to surface albedo  $(\frac{\partial RAD_{TOA}}{\partial \alpha})$   
 64 that we hereafter refer to as radiative sensitivity (RS) :

$$RI_{TOA,\alpha}(x,y) = \underbrace{\frac{d\alpha_{SI}}{dT_S}}_{IS(x,y)} \underbrace{\frac{\partial RAD_{TOA}(x,y)}{\partial \alpha(x,y)}}_{RS(x,y)}. \quad (2)$$

65 The normalization of  $RI_{TOA,\alpha}(x,y)$  by global mean temperature change is integrated into the IS  
 66 term and RS is defined as the local radiative change at the TOA per unit of surface albedo change.  
 67 This study considers only the radiative impact of  $\alpha$  changes in high latitudes (poleward of 60°N  
 68 and 55°S, in the northern (NH) and Southern (SH) hemispheres respectively) over oceans, and  
 69 calculations of SIAF exclude the impact of changes in terrestrial snow cover. **RS and  $\alpha$  changes**  
 70 **are calculated for each month and then their product is time averaged.** Changes in  $\alpha_{SI}$  are calcu-  
 71 lated over the ocean and capture both the impact of sea ice loss and changes in surface albedo over  
 72 sea ice (i.e. snow and melt ponds). Hall and Qu (2006) found that RS varies very little between  
 73 climate models. As a result, much of the literature on SIAF uncertainty has focused on processes  
 74 controlling sea ice albedo changes (Horvat et al. 2019) and the sensitivity of **sea ice concentration**  
 75 **(SIC)** to warming (Yu et al. 2006; Qu and Hall 2005; Curry et al. 1994) which both vary substan-  
 76 tially between models. The IPCC estimate of SIAF (Flato et al. 2013; Soden and Held 2006b)  
 77 used a RS calculated from a single model, neglecting inter-model differences and biases (relative

78 to observations) and assuming RS does not contribute to SIAF uncertainty. We assess the validity  
79 of this assumption below.

80 RS depends primarily on cloud reflectivity; clouds impede the amount of downwelling solar  
81 radiation reaching the surface and also reduce the amount of solar radiation reflected by the surface  
82 from reaching the TOA (Taylor et al. 2007; Donohoe and Battisti 2011) leading to a quadratic  
83 dependence of RS on cloud reflectivity. High latitude cloud properties vary substantially between  
84 models and exhibit many biases relative to observations (Gorodetskaya et al. 2006; Vavrus et al.  
85 2009; Trenberth and Fasullo 2010). Cloud differences can contribute to model differences in RS  
86 that in turn influence: (i) the sensitivity of sea ice loss to future warming (Hwang et al. 2011) via  
87 local positive radiative feedbacks and (ii) the impact of sea ice loss on the global energy budget  
88 and, thus, the global climate sensitivity to external forcing.

89 This study assesses inter-model differences in RS and consistency compared to estimates from  
90 satellite observations. We also identify relative contributions of IS and RS to model spread and  
91 biases (relative to observations) in the amplification of global warming by SIAF, and evaluate the  
92 impact of using RS from a single climate model to calculate SIAF across models as was done in  
93 Soden and Held (2006b) and the IPCC AR5 estimate of surface albedo feedback.

94 The manuscript is organized as follows: section 2, outlines how a simplified isotropic model  
95 often discussed in textbooks on radiative transfer, and further developed by Taylor et al. (2007)  
96 can be used to calculate RS from standard climate model output and demonstrates that the method  
97 reproduces results from more computationally demanding radiative kernel techniques. This fa-  
98 cilitates further evaluation of inter-model spread in RS in the coupled models participating in the  
99 Coupled Model Inter-comparison Project (CMIP3 and CMIP5 Meehl et al. 2007; Taylor et al.  
100 2012). Most importantly, this method also provides an observational estimate of RS from satellite  
101 data (Section 3). These estimates of RS along with the sea ice response over the historical period

102 are used to calculate an observational SIAF (Section 4). The observational SIAF is compared to  
103 that in model simulations under historical forcing and 4XCO<sub>2</sub> and the model spread and biases are  
104 decomposed into contributions from RS and IS (Section 5). A summary and discussion follows.

## 105 **2. The impact of surface albedo changes on TOA radiation in radiative kernels and a simpli-** 106 **fied model**

### 107 *a. Radiative kernels*

108 The impact of surface albedo changes on TOA radiation (RS) has been rigorously calculated  
109 using radiative kernel techniques in a small number of climate models (Smith et al. 2018; Pen-  
110 dergrass and Vitt 2018; Shell et al. 2008; Block and Mauritsen 2013; Soden and Held 2006b;  
111 Previdi 2010). RS can be calculated directly from offline radiative model calculations by prescrib-  
112 ing changes to the surface albedo ( $\alpha$ ) at each grid point and then running the radiative code with  
113 all other fields unchanged – a technique referred to as a radiative kernel calculation (Soden and  
114 Held 2006b; Shell et al. 2008). Radiative kernels are generally calculated over a global domain  
115 by perturbing the surface albedo at each grid point by a specified amount (independent of whether  
116 that surface albedo change is feasible) using atmospheric models with prescribed historical clima-  
117 tological (seasonally varying) sea surface temperatures. We use kernel calculations (for specific  
118 models) provided by: 1.) Karen Shell, NCAR CAM3 (Shell et al. 2008), 2.) Karoline Block,  
119 MPI ECHAM6 (Block and Mauritsen 2013), 3.) Angie Pendergrass, NCAR CAM5 (Pendergrass  
120 and Vitt 2018), 4.) Chris Smith, UKMO HadGEM2 (Smith et al. 2018), 5.) Brian Soden, GFDL  
121 AM2p12b (Soden and Held 2006b).

122 RS is reported in  $\text{W m}^{-2} \%^{-1}$  where the % refers to a 0.01 unit change in surface albedo  
123 (independent of the climatological surface albedo). Summertime (MJJA) daily-averaged TOA

124 insolation in the Arctic (defined as the region poleward of  $60^{\circ}N$ ) is of order  $420 \text{ W m}^{-2}$ , and a  
125  $4.2 \text{ W m}^{-2} \%^{-1}$  RS would be expected in a completely transparent atmosphere. Radiative kernel  
126 calculations produce an RS Arctic average of  $1.63 \text{ W m}^{-2} \%^{-1}$  across the 4 different models  
127 (numbers in the upper right of each panel in Fig. 1) indicating that the atmosphere attenuates  
128 the surface contribution to reflected radiation at the TOA by a factor of  $\sim 2.6$  ( $4.2/1.63$ ). Kernel  
129 estimates of RS in Arctic summer (May-June-July-August) are largest over Greenland ( $2\text{-}3.5 \text{ W}$   
130  $\text{m}^{-2} \%^{-1}$ ), smallest in the Greenland Iceland Norwegian (GIN) Seas ( $0.5\text{-}1 \text{ W m}^{-2} \%^{-1}$ ) with  
131 intermediate values in the central Arctic ( $1\text{-}2.5 \text{ W m}^{-2} \%^{-1}$  – Upper panels of Fig. 1). This  
132 spatial structure primarily reflects the climatological pattern of solar radiation reaching the surface  
133 in the Arctic (Lindsay et al. 2014). Highest RS values are found where cloud cover and water  
134 vapor are low over the high topography of Greenland. Moderate RS values are seen in the central  
135 Arctic due to the thin but persistent cloud cover over the perennial sea ice. RS is smallest in the  
136 GIN seas due to abundant thick clouds.

137 There is remarkable inter-model spread in Arctic RS across the different radiative kernel calcu-  
138 lations, especially over the central Arctic where the models differ by a factor of **two**. As shown  
139 below, the diversity of RS across the different kernel calculations is a consequence of inter-model  
140 differences in the mean state cloudiness and *not* due to differences in radiative transfer code or the  
141 methodology used to calculate the kernels between the different groups.

142 In the SO, RS during the Austral summer (NDJF) calculated from radiative kernels shows a  
143 zonally annular structure in all models with smaller values over the cloudy storm track region  
144 equatorward of the ice edge and larger values over the sea ice (upper panels of Fig. 2). However,  
145 the models differ to first order on the magnitude of RS over the open ocean and on the location  
146 and aerial extent of the region of larger RS adjacent to the Antarctic continent. In HADGEM2,  
147 the value of RS over the open ocean is  $2 \text{ W m}^{-2} \%^{-1}$  whereas in NCAR CAM3 RS is  $1 \text{ W m}^{-2}$

148  $\%^{-1}$  over the same region. In NCAR CAM5, the region of high RS adjacent to the Antarctic coast  
149 extends substantially into the SO whereas in NCAR CAM3 and ECHAM6 the high RS region  
150 is confined to the coast itself with the exception of the Weddel and Ross Seas. The inter-model  
151 differences in the aerial extent of the high RS region roughly correspond to inter-model biases in  
152 summertime ice extent; the gradient in atmospheric transmissivity is linked to the sea ice edge via  
153 cloud coverage and atmospheric water content although in some models the gradient in cloudiness  
154 is significantly poleward of the ice edge (i.e. NCAR CAM3) while in other models the cloud  
155 gradient is co-located with the ice-edge (i.e. NCAR CAM5). Overall, the SO domain average RS  
156 (excluding the Antarctic continent – to focus on the sea ice) ranges from 1.29 to 1.75  $\text{W m}^{-2} \%^{-1}$   
157 (as shown by the values in the upper right corner of Fig. 2).

### 158 *b. Isotropic single layer model*

159 Taylor et al. (2007) – hereafter T07– developed a model (hereafter the isotropic model) that can  
160 be used for approximating RS from the climatological radiative fluxes at the TOA and surface  
161 and some basic assumptions about shortwave radiative transfer in the atmosphere. Part of the T07  
162 derivation is repeated here for clarity with a few modifications to variable names. Of the incident  
163 shortwave radiation at the TOA ( $S$ ), assume a fraction ( $A$ ) is absorbed in the atmosphere above  
164 cloud top and a fraction  $R$  of the radiation incident on cloud top is reflected back to space (Fig.  
165 3). This resultant downwelling radiation at the surface is  $S(1-A)(1-R)$ . A fraction ( $\alpha$ , equal to  
166 the surface albedo) of this downwelling radiation is reflected upwards. Of this surface upwelling  
167 radiation,  $R$  is reflected back (downward) to surface with the remainder ( $S[1-A][1-R]^2$ ) transmit-  
168 ted to space. Reflections and transmissions are continued indefinitely subject to the three primary  
169 assumptions: (i) cloud optical properties can be represented by a single layer, (ii) cloud reflection  
170 is isotropic – the same fraction ( $R$ ) of broadband shortwave radiation incident on the cloud layer

171 is reflected independent of the direction (upwelling/downwelling) and how many previous inter-  
 172 actions with the surface and cloud occur and (ii) all of the atmospheric absorption occurs above  
 173 cloud top on the first downward pass which is apt for describing SW absorption by ozone in the  
 174 stratosphere (Chou and Lee 1996). We further analyze the limitations of these assumptions at the  
 175 end of this subsection.

176 In the isotropic model, loss of shortwave radiative energy from the climate system due to surface  
 177 albedo is a three step process: (i) insolation must be transmitted to the surface then (ii) reflected  
 178 by the surface and finally (iii) transmitted from the surface to the TOA. Mathematically, upwelling  
 179 SW radiation at the TOA that results from reflection off the surface is equal to the insolation  
 180 (S) times the downwelling transmissivity ( $[1 - A][1 - R]$ ) times the upwelling transmissivity (1-  
 181 R). The isotropic model also includes higher order reflections where the SW radiation reflected  
 182 at the surface is reflected back to the surface off clouds and thereafter will contribute additional  
 183 upwelling SW fluxes at the TOA with each subsequent reflection equal to the value of the previous  
 184 order contribution times  $\alpha R$ . These terms form an infinite geometric series that converges to the  
 185 expression:

$$SW \uparrow_{TOA} = \underbrace{SR(1-A)}_{SW \uparrow_{TOA,atmos}} + S\alpha \underbrace{\frac{(1-A)(1-R)^2}{1-\alpha R}}_{SW \uparrow_{TOA,surf}}, \quad (3)$$

186 where  $SW \uparrow_{TOA,atmos}$  and  $SW \uparrow_{TOA,surf}$  indicates the upwelling radiation at the TOA that was de-  
 187 rived from atmospheric and surface reflection respectively. Thus, if the values of R and A along  
 188 with  $\alpha$  and S are known, the contribution of the surface to the SW flux at the TOA can be cal-  
 189 culated. In our case, the isotropic model provides equations relating 3 satellite derived quantities  
 190 ( $SW \uparrow_{TOA}$ ,  $SW \uparrow_{SURF}$  and,  $SW \downarrow_{SURF}$ ) in terms of 3 unknown variables (A,R, $\alpha$ ) and the satellite  
 191 measured S. The result is a determined set of 3 equations in terms of 3 variables. Thus, the clima-

192 tological radiative fluxes allow the calculation of the single pass A and R for each climate model.  
 193 We can then calculate the expected change of  $SW \uparrow_{TOA}$  as  $\alpha$  changes with all else being equal by  
 194 taking the partial derivative of Eq. 3 with respect to  $\alpha$ .

$$RS = \frac{\partial SW \uparrow_{TOA}}{\partial \alpha} = S \frac{(1-A)(1-R)^2}{1-\alpha R} \left( 1 + \frac{R\alpha}{1-R\alpha} \right). \quad (4)$$

195 This provides an alternate method for calculating RS that relies only on readily available model  
 196 output at monthly resolution that can also be compared with the RS calculated from radiative  
 197 kernel techniques.

198 The lower panels of Fig. 1 show the RS in the Arctic summer calculated from Eq. 4 applied to  
 199 the monthly climatological output from the same control simulations that were used to calculate  
 200 the radiative kernels. The RS calculated from the isotropic model is in good agreement with that  
 201 calculated from radiative kernels in terms of the spatial pattern of RS and inter-model differences.  
 202 Spatial correlation between RS in the isotropic model and radiative kernel calculation for each  
 203 model is high with an  $R^2$  that exceeds 95% in all but NCAR CAM3. The inter-model differences  
 204 in domain average of RS is within 10% in the absolute sense and captures the rank of RS in models  
 205 (c.f. the adjacent upper and lower panels of Fig. 1 with  $R^2$  listed in the middle). The isotropic  
 206 model explains 94% of the variance in MJJA RS calculated from radiative kernels considered  
 207 across models and over all Arctic grid points collectively with a root mean squared (RMS) error  
 208 of  $0.15 \text{ W m}^{-2} \%^{-1}$  (top panel of supplemental Fig. A2). As a basis for comparison, if one used  
 209 the spatial pattern of MJJA RS calculated using radiative kernels from one model to predict the  
 210 kernel based RS in a different model – as was done in the IPCC estimate of SIAF– the RS variance  
 211 explained is 21% with a RMS error of  $0.67 \text{ W m}^{-2} \%^{-1}$  (bottom panel of Fig. A2). Thus, the  
 212 isotropic model offers a factor of 4 improvement on the practice of applying RS calculations from  
 213 a single climate model.

214 The isotropic model also captures the spatial pattern and inter-model spread of the kernel cal-  
215 culated RS in the SO (Fig. 2) although the absolute values of RS differs by as much as 20% (in  
216 the HADGEM2 model). The isotropic model explains 96% of the variance in NDJF kernel RS  
217 across models over the SO (top panel of supplemental Fig. A3) with a root mean squared (RMS)  
218 error of  $0.23 \text{ W m}^{-2} \%^{-1}$ . When radiative kernels from one model are used to predict the kernel  
219 based NDJF RS in a different model the variance explained is 71% with a RMS error of  $0.47 \text{ W}$   
220  $\text{m}^{-2} \%^{-1}$  (bottom panel of Fig. A3). Thus, the isotropic model offers a factor of 2 improvement  
221 on the practice of applying RS calculations from a single climate model in the SO. These results  
222 indicate that the isotropic model captures the essential SW radiative processes that determine the  
223 RS of surface albedo changes, and that the inter-model spread in RS is determined by the climato-  
224 logical cloud reflectivity which is adequately calculated from the modeled TOA and surface fluxes  
225 according to Eq. 3.

226 The isotropic model tends to bias the RS high relative to the radiative kernel (c.f. the domain av-  
227 erage values listed in the upper right of the map in the upper and lower panels of Figs. 1 and 2) and  
228 we speculate this results from the simplifying assumption that atmospheric absorption only occurs  
229 during the first pass as this allows more of the radiation reflected off the surface to be transmitted to  
230 space than would occur if the atmosphere absorbed upwelling solar radiation. Alternative formula-  
231 tions of similar isotropic models (Donohoe and Battisti 2011) assume the atmospheric absorption  
232 occurs in the same layer as the cloud reflection and occurs on all passes through the atmosphere to  
233 account for shortwave absorption by water vapor that occurs throughout the troposphere (Donohoe  
234 and Battisti 2013). This model better matches the RS calculated by radiative kernels in the tropics  
235 and mid-latitudes but substantially underestimates RS relative to the radiative kernel derived value  
236 at high latitudes (Appendix Fig. A1). We speculate that in the dry Arctic, the atmospheric absorp-  
237 tion is primarily by stratospheric ozone whereas in the lower latitudes water vapor also contributes.

238 For this reason, we choose to assume the absorption occurs only on the downward pass and return  
239 to possible impacts and improvements of this method in the discussion section.

### 240 *c. Causes of inter-model spread in RS*

241 What processes are responsible for the factor of 2 spread in modeled RS in Figs. 1 and 2? The  
242 ability of the isotropic model to reproduce the kernel based RS calculated for each model demon-  
243 strates that the mean state atmospheric opacity is the primary determinant. Generally speaking,  
244 RS is determined by how much insolation is transmitted to the surface and thus how much impact  
245 surface albedo changes have on reflected solar radiation. More specifically, RS is proportional  
246 to the atmospheric transmissivity squared with higher order modifications due to the impact of  
247 multiple reflections (Eq. 4). What then causes the inter-model spread in atmospheric opacity?

248 Clear sky surface albedo kernels (Fig. 4) have much larger magnitudes than their all-sky coun-  
249 terparts. The very similar spatial structures and absolute values in the four models with available  
250 kernel calculations have domain averages that differ by 2% from the multi-model mean, indicat-  
251 ing that 1) clear-sky processes are not responsible for the inter-model spread in all-sky RS and  
252 2) the different radiative transfer codes used in the climate models find a similar RS for a similar  
253 (clear-sky) mean-state.

254 The atmospheric opacity parameters – reflectivity and absorptivity– that come out of the  
255 isotropic model applied to the mean states of the different climate models are shown in Fig. 5. The  
256 all-sky reflectivity is subdivided into a clear-sky and cloud component by applying the isotropic  
257 model to the clear-sky mean state radiative fields (as in T07) to define a clear-sky reflectivity, and  
258 the cloud reflectivity is then defined as the all-sky minus clear-sky reflectivity. All climate models  
259 have very similar and nearly spatially uniform clear-sky reflectivity and all-sky absorptivity with  
260 Arctic domain average absolute differences from the model mean of order 0.02 fractional units.

261 The slight spatial structure in clear-sky reflectivity and absorptivity is consistent between climate  
262 models. Clear-sky reflectivity is larger near the North Pole consistent with enhanced Rayleigh  
263 scattering due to the shallower angle of incidence with latitude. Absorptivity is smaller over the  
264 thinner atmosphere above topography and drier continents consistent with reduced absorption by  
265 water vapor. In contrast to the consistency of absorption and clear-sky reflection between models,  
266 the cloud reflectivity differs substantially between models in both spatial structure and domain  
267 average values (which differ between models by over 0.20 fractional units). In general, regions of  
268 stronger cloud reflectivity have smaller RS values consistent with less downwelling solar radiation  
269 at the surface in cloudy regions. However, the anti-correlation between the spatial variability in RS  
270 and cloud reflectivity is significant but far from perfect ( $R \approx -.60$ ) within a given climate model  
271 due to the (comparable in magnitude) impact of the spatial structure of mean state albedo (Eq. 4)  
272 on the multiple reflection contribution to RS. On a broader scale, the Arctic domain average cloud  
273 reflectivity is very strongly anti-correlated ( $R=-0.99$ ) with the domain average RS indicating that  
274 Arctic averaged RS is primarily determined by the mean state cloud reflectivity.

### 275 **3. Observational estimate of radiative sensitivity to surface albedo changes and comparison** 276 **to coupled models**

277 Given the strong correspondence between RS calculated from radiative kernels and the isotropic  
278 model (Figs. 1 and 2), we can use the isotropic model to calculate RS from observational estimates  
279 of radiative fluxes at the TOA and surface and use these same fields (routinely available from model  
280 simulations) to assess model biases in RS and diagnose their role in the SIAF.

281 Observational estimates of climatological radiative fluxes are taken from the CERES EBAF  
282 surface product version 4.0 (Loeb and Coauthors 2018; Kato and Coauthors 2018) between 2000

283 and 2018. Climate model RS is estimated using the isotropic model for the last decade (1995-  
284 2005) of historical CMIP5 (Taylor et al. 2012) climate simulations forced. <sup>1</sup>

285 Maps of summer (MJJJ) RS estimated from satellite products and models are shown in Fig. 6.  
286 Three spatial averages of RS are also provided: (i) the whole domain poleward of 60°N (upper  
287 left corner in black) – observational value of  $1.79 \text{ W m}^{-2} \%^{-1}$ ; (ii) the Arctic ocean excluding  
288 land masses (lower right in blue) – observational value of  $1.68 \text{ W m}^{-2} \%^{-1}$  and; (iii) the spatial  
289 average over the sea ice (the spatial footprint and region varies between models, lower left in  
290 purple) – observational value of  $1.92 \text{ W m}^{-2} \%^{-1}$ . The observational RS is very similar to multi-  
291 model mean values (  $1.72$ ,  $1.65$  and,  $1.79 \text{ W m}^{-2} \%^{-1}$  over the entire Arctic domain, Arctic ocean  
292 and sea ice regions respectively). The models and observations generally agree on the spatial  
293 pattern of RS over the Arctic with high values over the Greenland ice sheet where the reduced  
294 mass of the atmosphere above the high topography is associated with enhanced atmospheric SW  
295 transmissivity, lower RS values over the GIN Sea and more spatially uniform RS values over the  
296 Central Arctic. The magnitude of RS differs substantially across models with domain average RS  
297 varying by almost a factor of two between the models, consistent with results from the radiative  
298 kernel based RS calculation (Fig. 1). The inter-model ( $2\sigma$ ) spread in Arctic average RS is  $0.57$ ,  
299  $0.53$  and,  $0.64 \text{ W m}^{-2} \%^{-1}$  over the full Arctic domain, Arctic ocean and climatological sea ice  
300 respectively.

301 The SO observational estimate of summertime (NDJF) RS is similar but slightly lower (domain  
302 average excluding the Antarctic continent of  $1.56 \text{ W m}^{-2} \%^{-1}$ ) than the multi-model mean ( $1.71$   
303  $\text{W m}^{-2} \%^{-1}$ ). All models and observations show an annular structure in RS with smaller values  
304 in the storm track region and larger values adjacent to the Antarctic continent over the sea ice  
305 (Fig. 7). RS differs substantially between models (order factor 2) in the storm track region and

---

<sup>1</sup>Most of the radiative kernel calculations discussed in Section 2 used “modern”, slightly differing time periods.

306 on the location and lateral extent of the high RS region adjacent to the continent. Some models  
307 (i.e. CSIRO MK5) also have zonal asymmetries in RS that are best characterized as a zonal  
308 wavenumber 1 pattern. The domain average RS values differ by less than the factor of 2 differences  
309 seen in the Arctic, but the local RS difference between models –especially in the storm track region  
310 – are of order a factor of 2. The inter-model ( $2\sigma$ ) spread in SO average RS is  $0.54 \text{ W m}^{-2} \%^{-1}$ ,  
311 comparable in magnitude to that over the Arctic domain and Arctic ocean.

312 These results collectively suggest that while CMIP5 ensemble average RS of high latitude ice  
313 loss is quite similar to that implied from observational constraints, models diverge substantially  
314 on the radiative impact of ice loss because of differences in atmospheric optical properties (i.e.  
315 clouds).

#### 316 **4. Observational estimate of ice albedo feedback**

317 The global ice albedo feedback (SIAF) is (the spatial average of) the product of the RS – the  
318 TOA radiative impact of surface albedo changes – and the ice sensitivity (IS) – the surface albedo  
319 change due to ice loss per unit of global warming (Eqs. 1,2). Thus, the RS calculated from the  
320 climatological radiative fluxes and the isotropic model in the previous sections along with esti-  
321 mates of IS from the observational record provide an observational estimate of the SIAF that can  
322 be compared to the SIAF calculated using the same methodology applied to CMIP5 simulations  
323 with historical and long term forcing. Furthermore, we can explicitly ask if the model spread (and  
324 potential bias relative to observations) in SIAF is explained by RS or IS spread.

325 The observational estimate of IS is calculated from the changes in decadal surface albedo of  
326 the Arctic ocean from 1982 to 2016 (2007-2016 average minus 1982-1991 average – Fig. 8)  
327 during each summer month divided by the global mean surface temperature change over the same  
328 time period. We use two different observational based data sets to calculate the change in surface

329 albedo over this time period : (i) sea ice concentration calculated by the National Snow and Ice  
 330 Data Center (Cavalieri et al. 1996) from passive microwave brightness measured by the Nimbus  
 331 7 satellite available from 1979-2016 and (ii) broadband (all-sky) surface albedo measured by the  
 332 Advanced Very High Resolution Radiometer (AVHRR) Polar Pathfinder (APP-X) extended data  
 333 set (Wang and Key 2005) that covers the 1982-2017 time period. The central estimate of our  
 334 observational based IS is the average of calculations from these two data sets (elaborated on below)  
 335 and our uncertainty estimates account for differences across the two data-sets.

336 The NSIDC sea-ice concentration changes are converted to a surface albedo change record by  
 337 multiplying the SIC changes by the albedo contrast between sea ice and open ocean ( $\Delta\alpha$ ), which  
 338 is assumed to be spatially and temporally invariant:

$$IS = \frac{dSIC}{[dT_S]} \Delta\alpha. \quad (5)$$

339 Eq. 5 assumes that changes in  $\alpha_{SI}$  are isolated to regions of sea-ice melt. NSIDC monthly maps of  
 340 the decadal average change in sea ice concentration are multiplied by an assumed surface albedo  
 341 contrast between the open ocean and sea ice ( $\Delta\alpha$ ) of 0.54 -assuming a typical ice  $\alpha$  of 0.6 (Hummel  
 342 and Reck 1979) and an ocean albedo of 0.06 (Hansen et al. 1983). This choice of typical ice  
 343 albedo is an average of snow covered sea ice found during the late spring and sea ice with melt  
 344 ponds in the late summer (see Fig. 9 of Perovich et al. 2002). This map of monthly NSIDC ice-  
 345 concentration derived surface albedo change and those derived from the APP-X (also monthly)  
 346 data are averaged to produce the observational best estimate of change in surface albedo (Fig. 8C)  
 347 – hereafter referred to as the Observational Best Estimate (OBE). Both products produce similar  
 348 estimates of surface albedo changes (Appendix Fig. A4). We use differences between the two  
 349 surface albedo data sets as well as the intra-decadal variability within each data set to calculate the  
 350 uncertainty in observational IS (Fig. 8D) as outlined in the Appendix.

351 Observational IS is calculated by normalizing OBE surface albedo changes by a global surface  
352 temperature change of  $0.7 \pm 0.1\text{K}$  over the 1982-2016 time period. The central estimate and  
353 uncertainty in global mean surface temperature change come from the average and standard devi-  
354 ation of the mean across three different global surface temperature data sets: (i) National Centers  
355 for Environment Prediction (NCEP) reanalysis surface air temperature (Kalnay et al. 1996), (ii)  
356 the Goddard Institute for Space Studies Surface Temperature Analysis (GISTEMP) (Hansen et al.  
357 1999), and (iii) the modification by Cowtan and Way (Cowtan and Way 2014) of the Met Office  
358 Hadley Centre surface temperature dataset (Morice et al. 2012) version 4 (HadCRUT4).

359 The monthly IS is then multiplied by the monthly RS derived from CERES data, and then time  
360 averaged (over the summer months) to produce a map of radiative impact of sea ice changes (Fig.  
361 8E). While the previous figures showed MJJA average in the NH and NDJF in the SH, figure 8E ex-  
362 tends the summertime season to include the six months centered on the summer solstice (AMJJAS  
363 in NH and ONDJFM in the SH) since previous work (Flanner et al. 2011) found an appreciable  
364 contribution to the SIAF during the shoulder seasons especially in April. The uncertainty in the  
365  $RI_{TOA,\alpha}$  is (Fig. 8F) is assessed from a Monte Carlo simulation that takes into account 3 different  
366 uncertainties in the input data sets propagated (in quadrature) onto the calculation of  $RI_{TOA,\alpha}$  (see  
367 Appendix for details): (i) the uncertainty in RS – due to uncertainty in the climatological radiative  
368 fluxes, (ii) uncertainty in the surface albedo change – due to both intra-decadal variability and  
369 differences between the APP-X and NSIDC ice concentrations data sets and (iii) uncertainty in the  
370 global mean temperature change that goes into the calculation of IS. We note that  $RI_{TOA,\alpha}$  in Fig.  
371 8E is, by definition, the radiative impact of sea ice changes normalized by global mean surface  
372 temperature change ( $=0.7\text{K}$ ) and has a summertime (AMJJAS) Arctic domain average of  $4.9 \pm$   
373  $1.4 \text{ W m}^{-2} \text{ K}^{-1}$  which translates to an absolute change in summertime radiation of  $3.4 \pm 1.0 \text{ W}$   
374  $\text{m}^{-2}$  over the Arctic. To convert this number to a global and annual mean radiative impact, one

375 must weight this number by the ratio of summer months to the year ( $\frac{6}{12}$ ) and the spatial area of the  
376 Arctic (poleward of  $60^\circ\text{N}$ ) divided by that of the globe (.065) resulting in a global TOA radiative  
377 change of  $0.11 \text{ W m}^{-2}$  over the 1982-2016 period. This translates to a global radiative feedback  
378 of  $0.16 \pm 0.04 \text{ W m}^{-2} \text{ K}^{-1}$  given the observed global surface temperature change over the same  
379 period. The uncertainties cited above reflect 2 standard deviations.

380 We do not estimate the observational based surface albedo feedback in the SO because the  
381 change in SO sea ice concentration over the observational period is not statistically significant  
382 above the year-to-year variability (Jones and Coauthors 2009). We also note that this estimate is  
383 isolated to the Arctic ocean (we have masked the APP-X albedo changes over land) and, thus, does  
384 not include the impact of changes in snow cover over land.

## 385 **5. Comparison of observational and model SIAF and decomposition of inter-model spread** 386 **of SIAF into RS and IS**

387 We now compare the observational Arctic SIAF derived above with that derived by the same  
388 methodology in historical CMIP5 simulations. The RS for each climate model that was calculated  
389 using the isotropic model in the previous section (from the climatology at end of the historical  
390 simulation – 1995 to 2005) is multiplied by the decadal average surface albedo change –calculated  
391 as the ratio of upwelling to downwelling broadband shortwave radiation at the surface – over  
392 the historical simulation (1995 to 2005 minus 1975 to 1985). We note that this time period was  
393 chosen to correspond to the end of the historical simulations and differs from the 1982 to 2016  
394 period used for the observational calculations. The RS and surface albedo changes are calculated  
395 for each month and the product is spatially averaged over the Arctic ocean to calculate the SIAF;  
396 we exclude the impact of changes in snow cover over land from our calculations. For simplicity,  
397 we will only discuss the annual and global mean of the calculations normalized by the global

398 mean surface temperature change over the same time period, as we did for the observations. The  
399 CMIP5 ensemble mean Arctic SIAF in the historical simulations is  $0.12 \text{ W m}^{-2} \text{ K}^{-1}$  with a spread  
400 ( $2$  standard deviations,  $\sigma$ ) of  $0.13 \text{ W m}^{-2} \text{ K}^{-1}$  (gray histogram in Fig. 9A with wide bars). The  
401 ensemble mean is slightly smaller than the observational estimate (c.f the solid and dashed vertical  
402 black lines in Fig. 9) but the large inter-model spread indicates that the models differ in either RS  
403 and/or IS. We now ask how much RS and IS contribute to the inter-model differences in Arctic  
404 SIAF.

405 To estimate the IS contribution to the SIAF spread, the calculation of SIAF is repeated but the  
406 model specific RS is replaced with the observational based RS value. The resulting distribution of  
407 SIAF (blue histogram in Fig. 9A) shows the spread produced by biases and inter-model differences  
408 in IS. The mean value of SIAF in the fixed RS distribution ( $0.12 \text{ W m}^{-2} \text{ K}^{-1}$  – Table 1) is nearly  
409 equal to that of the full SIAF calculation (c.f. the blue and black vertical lines). The CMIP5  
410 ensemble average SIAF is quite insensitive to RS model biases, and it is lower than the observed  
411 estimate because the modeled IS is smaller than the observational estimate. Furthermore, the  
412 spread in the fixed RS distribution is only slightly smaller than that of the full SIAF calculation  
413 ( $2\sigma = 0.12 \text{ W m}^{-2} \text{ K}^{-1}$ ) indicating that the majority of the inter-model spread in SIAF calculated  
414 from the historical simulation is a result of the IS differences between models.

415 A similar analysis can be made to estimate the impact of biases (relative to observations) and  
416 inter-model RS differences on the calculated SIAF by replacing the model specific IS with that  
417 derived from observations (red histogram in Fig. 9A). The CMIP5 ensemble average SIAF of the  
418 fixed IS distribution ( $0.16 \text{ W m}^{-2} \text{ K}^{-1}$  – Table 1) is larger than that of the full SIAF calculation  
419 (c.f. the red and black vertical lines in Fig. 9) indicating that the CMIP5 ensemble average IS  
420 is smaller than that observed (the OBE value) a result also found by Rosenblum and Eisenman  
421 (2016). The inter-model spread in SIAF in the fixed IS experiment ( $2\sigma = 0.04 \text{ W m}^{-2} \text{ K}^{-1}$ )

422 is smaller than that of the full calculation and fixed RS experiment indicating that inter-model  
423 differences in RS play a smaller but not insignificant role in the SIAF spread calculated over the  
424 historical simulations. A summary of the role of biases and inter-model differences in RS and IS  
425 in determining the model distribution of SIAF is provided in Table 1.

426 This partitioning of SIAF differences in contributions from RS and IS takes spatial and temporal  
427 co-variances of ice loss and RS into account by weighting the ice loss to the RS at that location  
428 and time. Similar results for the impact of IS and RS on the total spread in SIAF are obtained by  
429 simply noting the fractional spread (relative to the ensemble mean) of summertime Arctic domain  
430 average RS and IS between models. The ratio of domain and summertime average inter-model  
431 spread ( $2\sigma$ ) to the ensemble mean domain and summertime average of RS is 40% whereas that  
432 of IS is 107% roughly scaling with the fractional contribution to SIAF spread calculated above.  
433 This result suggests that inter-model differences in IS and RS are fairly spatially and temporally  
434 homogenous and the resultant inter-model spread in SIAF is independent of the spatiotemporal  
435 co-variability of RS and IS. Previous work has found similar large magnitude inter-model spread  
436 in IS in CMIP3 (Mahlstein and Knutti 2012) and CMIP5 (Stroeve and Notz 2015) linked to the  
437 spread in the magnitude of Arctic amplification.

438 The sea ice retreat over the historical record represents the superposition of the response to cli-  
439 mate forcing and natural variability and, thus, the inter-model spread in IS calculated over the  
440 30 years of historical simulations is expected to exceed that in response to long-term sustained  
441 forcing. Schneider et al. (2018) found that decadal trends in sea-ice during periods when global  
442 mean temperatures increased by more than 0.5K provided good estimates of the long-term SIAF  
443 in an ensemble of climate models. Other studies suggest that 60% of the observed Arctic sea loss  
444 since 1979 is a result of the natural variability of atmospheric circulation (Ding et al. 2017, 2019)  
445 and that trends in sea ice differ by as much as 50% at the multi-decadal timescale in model en-

446 sembles due to natural variability (Kay et al. 2011). To reduce the amount of internal variability  
447 relative to the forced component, we also look at the contribution of RS and IS to the inter-model  
448 spread in SIAF in response to an abrupt and sustained quadrupling of atmospheric CO<sub>2</sub> where the  
449 forced climate change signal is expected to be larger than the natural variability. The IS in the CO<sub>2</sub>  
450 quadrupling simulations is calculated from the change in surface albedo and global mean surface  
451 temperature between the PI and the average over years 50-100 since CO<sub>2</sub> quadrupling. The RS  
452 used to calculate the SIAF is calculated from the PI climatological fields in the same model. The  
453 ensemble average Arctic SIAF calculated from the 4XCO<sub>2</sub> simulations is  $0.13 \pm 0.09 \text{ W m}^{-2} \text{ K}^{-1}$   
454 (uncertainty is  $2\sigma$ ) and is in close agreement with the ensemble average of the historical simula-  
455 tion ( $0.12 \pm 0.13 \text{ W m}^{-2} \text{ K}^{-1}$ ) with reduced inter-model spread. The central estimate and range  
456 of SIAF from all model simulations – calculated from  $2\sigma$  of the mean – is  $0.13 \pm 0.02 \text{ W m}^{-2} \text{ K}^{-1}$   
457 and is slightly smaller than but not statistically different from the observational estimate ( $0.16 \pm$   
458  $0.04 \text{ W m}^{-2} \text{ K}^{-1}$ ). Because the 4XCO<sub>2</sub> ice response primarily reflects the forced response, the  
459 similarity of the ensemble average SIAF diagnosed from historical and 4XCO<sub>2</sub> simulations sug-  
460 gests that the same physics responsible for the long-term SIAF are evident in historical simulations  
461 despite the additional statistical noise from internal variability.

462 When the model specific RS is replaced by the observational estimate of RS the resultant Arctic  
463 SIAF for the CO<sub>2</sub> quadrupling simulations is  $0.13 \pm 0.08 \text{ W m}^{-2} \text{ K}^{-1}$  and when the model specific  
464 IS is replaced by the observational estimate of IS the resultant SIAF is  $0.16 \pm 0.04 \text{ W m}^{-2} \text{ K}^{-1}$   
465 (lower left panel of Fig. 9 and Table 1). These results suggest that in the long-term response to  
466 sustained anthropogenic forcing: 1.) the CMIP5 ensemble average RS (spatially and temporally  
467 weighted by the relevant regions of ice loss) is very near the observational estimate, 2.) the CMIP5  
468 ensemble average IS (spatially and temporally weighted by structure of RS) is slightly smaller  
469 than the observational estimate and is responsible for the model SIAF being smaller than the

470 observational estimate and 3.) inter-model differences in IS contribute twice as much to the inter-  
471 model spread in SIAF (63% of the ensemble average value) than do inter-model differences in  
472 RS (30% of the ensemble average value). We note that, the inter-model spread in IS and RS are  
473 significantly ( $R=0.54$ ) correlated (at 95% confidence interval) and return to the implication of this  
474 result in the discussion section.

475 A similar analysis can be performed for the  $4XCO_2$  simulations in the SO (poleward of  $55^\circ S$ ) to  
476 indicate an ensemble average SIAF of  $0.08 \pm 0.13 \text{ W m}^{-2} \text{ K}^{-1}$  (Fig. 9C, Table 1). The SO SIAF  
477 is negative in a single model (GFDL ESM2G) that simulates sea ice growth in the Weddell Sea  
478 under  $4XCO_2$ . When the model specific RS is replaced by the observational estimate of RS, the  
479 calculated SO SIAF is  $0.07 \pm 0.11 \text{ W m}^{-2} \text{ K}^{-1}$  suggesting the the ensemble average RS is slightly  
480 larger than that estimated from the observations, consistent with Fig. 7. Because no observational  
481 estimate of SO IS is available, we probe the sensitivity of SO SIAF to RS by replacing the model  
482 specific IS with the ensemble average IS resulting in a calculated SIAF of  $0.08 \pm 0.04 \text{ W m}^{-2} \text{ K}^{-1}$ ;  
483 inter-model differences in RS result in inter-model differences in SO SIAF of magnitude 50% the  
484 ensemble mean estimate. However, the contribution of inter-model spread in RS to SIAF spread is  
485 dwarfed by the impact of inter-model differences in IS which produces inter-model differences in  
486 SO SIAF exceeding the central estimate by almost a factor of 1.5 (160%). This result is consistent  
487 with the large inter-model differences in SO ice response to global warming reported by Shu et al.  
488 (2015); Polvani and Smith (2013).

#### 489 *a. Global surface albedo feedback – comparison to IPCC AR5 value*

490 The IPCC AR5 estimated a global surface albedo feedback of  $0.26 \text{ W m}^{-2} \text{ K}^{-1}$  based on the  
491 calculations of Soden and Held (2006b) which use a single RS – derived from kernel calculations  
492 in the GFDL model (Fig. 1) – applied the surface albedo change in each CMIP3 model. [More](#)

493 recently, Schneider et al. (2018) presented a CMIP5 ensemble mean IAF  $0.40 \text{ W m}^{-2} \text{ K}^{-1}$  using  
494 NCAR CAM5 based kernels. It is unclear if this discrepancy result from the different RS used in  
495 these studies or the IS in different GCM ensembles. Here, we compare the SIAF produced using  
496 the (kernel based) RS from a single model to that calculated using a model specific RS derived  
497 from the isotropic model. These calculations are global and include the impact of  $\alpha$  changes over  
498 land (due to changes in snow cover) in addition to the sea-ice related changes considered up to this  
499 point and we term this combined contribution of land and sea ice changes the ice-albedo feedback  
500 (IAF).

501 Our IAF calculations are based upon surface albedo change calculated from the  $4\text{XCO}_2$  simula-  
502 tions minus that in the PI simulation normalized by the global mean surface temperature change in  
503 that model – a quantity akin to IS in Eq. 2 but including the albedo changes over land. This albedo  
504 change is multiplied by RS estimated two ways: (i) using the method introduced in this study,  
505 where RS is calculated from the isotropic model (Eq. 4) using radiative fluxes from appropriate  
506 model specific PI simulation and (ii) using the method introduced by Soden and Held (2006b)  
507 where the GFDL surface albedo kernel (Fig. 1) is used to estimate RS for all models. We separate  
508 the IAF calculation into hemispheres. In the NH, the IAF calculated in this study is larger than  
509 that calculated using the GFDL kernel in all models (all the red dots fall below the 1:1 line in the  
510 upper left panel of Fig. 10) as would be expected from the GFDL RS being at the very low end of  
511 the model range especially over the ocean domain. In the CMIP5 ensemble average, the NH IAF  
512 is  $0.20 \text{ W m}^{-2} \text{ K}^{-1}$  using the GFDL kernel as compared to  $0.27 \text{ W m}^{-2} \text{ K}^{-1}$  using the isotropic  
513 model methodology (35% greater – Table 2). The NH IAF has 64% more spread using the model  
514 specific RS because: (i) the ensemble mean RS is larger than the GFDL kernel RS and (ii) the  
515 inter-model spread in RS contributes to the IAF spread as discussed in the previous subsection. If  
516 we restrict the calculation to the Arctic ocean poleward of  $60^\circ\text{N}$  (as was done in Sections 4 and 5)

517 we find a CMIP5 ensemble average SIAF of  $0.09 \text{ W m}^{-2} \text{ K}^{-1}$  using the GFDL kernel compared to  
518 the  $0.13 \text{ W m}^{-2} \text{ K}^{-1}$  (Table 1) using the isotropic model methodology (45% greater). This result  
519 suggests that approximately half of the IAF is due to  $\alpha$  changes over land as found by Flanner  
520 et al. (2011).

521 In the Southern Hemisphere, the IAF estimates from the two methods are in closer agreement;  
522 the dots cluster along near the 1:1 line in the upper right panel of Fig. 10 with the exception of the  
523 models producing the highest IAF. This result is expected since the GFDL RS is near the ensemble  
524 mean over the SO (Fig. 2 and Fig. 7). The ensemble average IAF in the SH is, therefore, very sim-  
525 ilar when using the methodology in this study ( $0.09 \text{ W m}^{-2} \text{ K}^{-1}$ ) as compared to that calculated  
526 using GFDL RS only ( $0.08 \text{ W m}^{-2} \text{ K}^{-1}$ ) – Table 2. Globally, we calculate an IAF of  $0.37 \text{ W m}^{-2}$   
527  $\text{K}^{-1}$  which is 30% greater than the same result found applying the GFDL RS to CMIP5 4XCO<sub>2</sub>  
528 simulations of  $0.29 \text{ W m}^{-2} \text{ K}^{-1}$ . We note the the IPCC AR5 cites a global IAF of  $0.26 \text{ W m}^{-2}$   
529  $\text{K}^{-1}$  derived from the GFDL kernel and CMIP4 simulations and, thus, our estimate is 40% larger  
530 than the AR5 value. We attribute 30% of this increase to improved methodology of using model  
531 specific RS and 10% to the difference between CMIP4 and CMIP5 model characteristics. **Import-**  
532 **antly, the IPCC diagnosis of the overall climate sensitivity of climate models is unaffected by our**  
533 **revised more positive IAF. Rather, our results suggest that the shortwave cloud feedback should be**  
534 **revised downward by the same amount because cloud feedbacks are diagnosed from all-sky minus**  
535 **clear-sky TOA radiation adjusted by all-sky minus clear-sky radiative kernel calculations.**

## 536 6. Summary and discussion

537 We have shown that the radiative impact of surface albedo changes (RS) calculated using of-  
538 fline radiative transfer models (radiative kernels) can be closely replicated using a single layer  
539 isotropic SW radiation model applied to the climatological radiative fluxes at the TOA and sur-

540 face. This procedure allows estimates of SIAF to be conveniently calculated from observational  
541 data sets and standard model output without use of a kernel calculation, facilitating a comparison  
542 of observational and model estimates of SIAF. It also allows the differences between models and  
543 observations based calculations to be decomposed into contributions from RS and IS. The multi-  
544 model mean of RS is close to the observational estimate in the Arctic and only slightly larger than  
545 the observational estimate in the SO. However, the inter-model spread in RS (Figs. 6 and 7) is  
546 substantial, producing inter-model differences in SIAF estimates that are 30% and 50% the mag-  
547 nitude of the ensemble mean SIAF in the Arctic and SO respectively. In agreement with Sledd  
548 and L'Ecuyer (2019), high latitude clouds tend to mask the impact of surface albedo variations on  
549 the TOA albedo by a factor of 2-3 in observational estimates. Differences in climate model clouds  
550 influence the degree of cloud masking.

551 Our results indicate that inter-model differences in IS are more important than RS in explaining  
552 the inter-model spread in SIAF. However, IS is not statistically independent of RS ( $R = 0.54$ ). It  
553 is possible that inter-model differences in RS contribute to inter-model difference in IS because  
554 models that have a larger radiative response to sea ice loss will tend to have greater sea ice loss  
555 due to a stronger positive feedback between initial ice loss and radiative heating. In this sense, the  
556 contribution of RS to inter-model differences in SIAF of  $0.04$  and  $0.04 \text{ W m}^{-2} \text{ K}^{-1}$  in the Arctic  
557 and SO respectively can be thought of as a lower bound on the contribution of mean state radiative  
558 biases to the SIAF. We hope to explore the impact of mean state radiative biases (RS) on IS and  
559 the persistence of sea ice loss events in future work.

560 We estimate an observationally based global, and annually averaged increase in TOA radiation  
561 of  $0.11 \text{ W m}^{-2}$  from Arctic sea ice changes over the 1982-2016 time period using observationally  
562 based estimates of sea ice changes and the CERES derived radiative sensitivity (RS) implying a  
563 SIAF of  $0.16 \pm 0.04 \text{ W m}^{-2} \text{ K}^{-1}$ . Flanner et al. (2011) found a Northern Hemisphere average

564 "cryospheric radiative forcing" of  $0.45 \text{ W m}^{-2}$  over the 1979-2008 time period about half of  
565 which ( $0.22 \text{ W m}^{-2}$ ) was attributed to sea ice changes – the other half was attributed to snow  
566 changes over land. Thus, the Flanner et al. (2011) result converted to a global average ( $0.22/2$   
567  $=0.11 \text{ W m}^{-2}$ ) agrees very well with our findings. Similarly, (Cao et al. 2015) found a Northern  
568 Hemisphere SIAF of  $0.25 \text{ W m}^{-2} \text{ K}^{-1}$  using observed surface albedo change and RS estimated  
569 using model based kernels derived from GFDL (Soden and Held 2006b) and CAM3 (Shell et al.  
570 2008). This result translates to a global feedback of Arctic changes of  $0.12 \text{ W m}^{-2} \text{ K}^{-1}$  which is  
571 smaller than our central estimate and we speculate this result follows from the lower than observed  
572 RS in the CAM3 kernel (Fig. 1).

573 Pistone et al. (2014, 2019) calculated a substantially larger SIAF ( $0.31 \pm 0.04 \text{ W m}^{-2} \text{ K}^{-1}$ ) from  
574 the inter-annual covariance of sea ice concentration and TOA radiation measured by CERES. We  
575 speculate that some of the TOA radiative variability that coincides with ice loss events in Pistone  
576 et al. (2014) is not directly a consequence of (i.e. geographically co-located with and/or a radiative  
577 consequence) surface albedo changes but, rather, is a consequence of atmospheric optical proper-  
578 ties (i.e. clouds, water vapor, etc) that co-vary with Arctic sea ice concentration. A central question  
579 moving forward is whether the atmospheric changes (and the associated radiative anomalies) ac-  
580 companying Arctic sea ice loss over the limited historical period result from natural variability of  
581 atmospheric circulation initiated by tropical and mid-latitude processes or are a direct result of sea  
582 ice loss and, thus, should be expected to also apply to future climatological changes. Additionally,  
583 how accurately does the observational IS calculated over the historic record represent the expected  
584 relationship between future changes in Arctic ice concentration and global mean temperature?

585 Pistone et al. (2014) suggest that the SIAF alone results in a 25% enhancement of global warm-  
586 ing via radiative feedbacks, a value they derive from the ratio of their calculated radiative impact  
587 of historic ice loss divided by the anthropogenic climate forcing to date. We offer two modifi-

588 cations as updates to their calculation: (i) a significantly lower estimate of the radiative impact  
 589 of Arctic sea ice loss outlined above and (ii) consideration of how the implied feedback relates  
 590 to equilibrium climate sensitivity, noting that the climate system is not currently in equilibrium  
 591 with the anthropogenic forcing to date. For the latter reason, the feedback gain of the Arctic SIAF  
 592 should be calculated by comparing the SIAF to the equilibrium radiative feedback of all other  
 593 radiative processes as opposed to the ratio of the transient radiative impact of ice loss to date to  
 594 the applied forcing. Given observational central estimates of the total equilibrium feedback pa-  
 595 rameter of  $-1.19 \text{ W m}^{-2} \text{ K}^{-1}$  (Armour 2017) and our observational estimate of the Arctic SIAF  
 596 ( $\lambda_{SIAF} = +0.16 \pm 0.04 \text{ W m}^{-2} \text{ K}^{-1}$ ) the implied feedback parameter of all processes excluding  
 597 the SIAF ( $\lambda_0$ ) satisfies the equation  $-1.19 \text{ W m}^{-2} \text{ K}^{-1} = \lambda_0 + 0.16 \text{ W m}^{-2} \text{ K}^{-1}$ . This implies that  
 598  $\lambda_0$  (the reference climate feedback parameter of a system with no SIAF) is  $-1.35 \text{ W m}^{-2} \text{ K}^{-1}$ . We  
 599 note that the reference climate feedback parameter is more negative than that of a system with a  
 600 SIAF implying a smaller climate sensitivity of the reference system relative the full system with a  
 601 SIAF as is expected for the positive SIAF. The fractional amplification of global mean temperature  
 602 changes – the feedback gain,  $G_{SIAF}$ – due to the SIAF is then (Roe 2009):

$$G_{SIAF} = \frac{1}{1 + \frac{\lambda_{SIAF}}{\lambda_0}} = 1.14 \pm .04. \quad (6)$$

603 Thus, our analysis suggests that the Arctic SIAF amplifies global warming by 14% ( $2\sigma$  range be-  
 604 tween 10 and 19%) at the equilibrium timescale and is a more modest amplifier of global warming  
 605 than the 25% suggested by Pistone et al. (2014).

606 The IPCC AR5 report (Flato et al. 2013) points out a discrepancy between the observational  
 607 based SIAF of Flanner et al. (2011) and the model based estimate of Soden and Held (2006b)  
 608 and speculates that models are biased toward low IS, but the role of inter-model spread and biases  
 609 in RS were neglected. While we find no ensemble mean model bias in Arctic RS (Fig. 6), the

610 model estimate of RS used in Soden and Held (2006b) is taken from radiative kernel calculations  
611 in a single (GFDL) model and then applied to the IS across models. The RS from that model  
612 (Fig. 1) is biased low relative to both the observational based RS (by 46% of the kernel RS in  
613 the Arctic average) and the CMIP5 ensemble mean. As a result, the AR5 estimate of the global  
614 surface albedo feedback of  $0.26 \text{ W m}^{-2} \text{ K}^{-1}$  based on the calculations of Soden and Held (2006b)  
615 is substantially lower than our calculated value of  $0.37 \text{ W m}^{-2} \text{ K}^{-1}$  which uses model specific RS  
616 estimates. This result suggests that at least some part of the low model bias identified in the IPCC  
617 AR5 is a consequence of using a RS that is inconsistent with some climate models. We recommend  
618 using model specific RS derived from the isotropic model as a better practice to applying radiative  
619 kernels across models. Additionally, our results identified no discernible model bias in the SIAF  
620 at least when considering like quantities over the Arctic ocean domain.

621 *Acknowledgments.* We thank Karen Shell and 3 anonymous reviewers for thoughtful critique of  
622 an earlier version of this manuscript. We thank Angeline Pendergrass, Chris Smith, Ryan Kramer,  
623 Karen Shell, Brian Soden, Block and Marotzke and Michael Previdi for providing radiative kernel  
624 calculation and their assistance providing further clarification on the appropriate climatological  
625 radiation fields to use for isotropic model calculations. We also thank Jeff Key and Xuanji Wang  
626 for providing the NOAA AVHRR Polar Pathfinder data. This work was funded by a Department  
627 of energy mini grant to the HLES team at PNNL, the NSF Antarctic Program Grant Number PLR  
628 1643436 and the NOAA MAPP grant eGC1#A127135.

## 629 APPENDIX

630 We describe the methodology used to calculate the uncertainty in our observational estimates  
631 of the RS, IS and  $RI_{TOA,\alpha}$  the spatial average of which gives the resultant SIAF (Eq. 1). We  
632 do so by first bootstrapping (random re-sampling with replacement) the original observational

633 data into subsets half the temporal length of the original data to produce an ensemble of records.  
634 For example, in the CERES data used to calculate the RS, we produce an ensemble of radiative  
635 climatologies derived from random selections of 9 years of the 18 years of data. This procedure  
636 queries how sensitive the radiative climatologies are to the limited length of the CERES record.  
637 Similarly, the surface albedo changes are calculated from the difference of random selections of  
638 5 year averages within the period 1982-1991 and 2007-2016. We then use the re-sampled data to  
639 calculate the RS – using the isotropic model– and IS in a Monte-Carlo simulation. We calculate  
640 100 different estimates of RS and 100 different estimates of IS with 50 derived from re-sampled  
641 NSIDC ice concentration data and 50 derived from re-sampled APP-X data. Thus, our estimates  
642 of IS (Fig. 8D) account for two sources of uncertainty: (i) the impact of intra-decadal variability  
643 on calculating longer term changes in surface albedo and (ii) instrumental uncertainty.

644 The within data set intra-decadal variability of surface albedo contributes more to the IS uncer-  
645 tainty than the differences between APP-X and NSIDC sea ice concentration data sets; the standard  
646 deviation in IS calculated from ensembles of just the 50 NSIDC or 50 APP-X data is similar to that  
647 derived from the 100 member ensemble considered collectively. Given that the NSIDC estimate  
648 of surface albedo change is derived from sea ice concentration changes only and does not account  
649 for changes in the albedo over ice, the similarity of the NSIDC and APP-X derived IS suggest that  
650 albedo changes are primarily associated with changes in ice area, in opposition to the findings of  
651 (Horvat et al. 2019). The uncertainty in RS (taken as 2 standard deviation across the re-sampled  
652 ensemble) is approximately 10% of the mean RS with larger values in the vicinity of sea ice edge  
653 (Fig. 8B) suggesting that the cloud properties that determine the RS are fairly constant from year-  
654 to-year. In contrast, the uncertainty in the IS (Fig. 8D) is approximately 60% of the mean value  
655 with particularly large uncertainties in the Beaufort Sea suggesting that the intra-decadal variabil-

656 ity and measurement uncertainty of sea ice changes substantially hinders the calculation of long  
657 term IS over the relatively short observational record.

658 We now describe how we use the uncertainty in IS and RS to calculate the uncertainty in  $RI_{TOA,\alpha}$ ,  
659 the spatial average of which gives the SIAF uncertainty. We diagnose uncertainty  $RI_{TOA,\alpha}$  by  
660 convoluting the 100 estimates of RS and the 100 estimates in IS to produce 10,000 estimates of  
661  $RI_{TOA,\alpha}$ . This procedure accounts for the spatial co-variance of IS and RS uncertainty and central  
662 estimates. For example, the uncertainty in IS will have a larger impact in the regions and seasons  
663 where RS is largest. The uncertainty in the  $RI_{TOA,\alpha}$  looks like and is comparable in fractional  
664 magnitude to that in surface albedo change with a slight modification by the spatial pattern of  
665 the mean RS. The spread in the spatial average of these 10,000  $RI_{TOA,\alpha}$  is combined with the  
666 uncertainty in global mean temperature changes – propagated in quadrature since both quantities  
667 are scalars– to produce a probability distribution function of SIAF (dark black distribution in left  
668 panels of Fig. 9). These calculation give an Arctic SIAF of  $0.14 \pm 0.4 \text{ W m}^{-2} \text{ K}^{-1}$  where the  
669 uncertainty is taken as  $2\sigma$ .

670 The uncertainty in the observational global SIAF can be decomposed into contributions from the  
671 RS and IS uncertainty as follows: (i) the contribution of RS is calculated as  $2\sigma$  of the distribution  
672 derived from the 100 estimates of RS and multiplied by the OBE IS and (ii) the contribution of IS  
673 is calculated as  $2\sigma$  of the distribution derived from the 100 estimates of IS and multiplied by the  
674 mean RS. The uncertainty in the observational SIAF is almost entirely ( $\pm 0.04 \text{ W m}^{-2} \text{ K}^{-1}$ ) due  
675 to uncertainty in the IS (dark blue narrow distribution in Fig. 9) whereas the uncertainty in the RS  
676 contributes very little to the global uncertainty in the SIAF ( $\pm 0.003 \text{ W m}^{-2} \text{ K}^{-1}$  – the very narrow  
677 dark red distribution in the left Fig. 9A).

678 **References**

- 679 Armour, K., 2017: Energy budget constraints on climate sensitivity in light of inconstant feed-  
680 backs. *Nat. Clim. Chang.*, **7**, 331–335.
- 681 Block, K., and T. Mauritsen, 2013: Forcing and feedback in the pi-esm-lr coupled model under  
682 abruptly quadrupled CO<sub>2</sub>. *J. Adv. Model. Earth Sy.*, **5** (4), 676–691.
- 683 Bony, S., and Coauthors, 2006: How well do we understand climate change feedback processes?  
684 *J. Climate*, **19**, 3345–3482.
- 685 Budyko, M., 1969: The effect of solar radiation variations on the climate of the earth. *Tellus*, **21**,  
686 611–619.
- 687 Cao, Y., S. Liang, X. Chen, and T. He, 2015: Assessment of sea ice albedo radiative forcing and  
688 feedback over the northern hemisphere from 1982 to 2009 using satellite and reanalysis data. *J.*  
689 *Climate*, **28**, 1248–1259, doi:10.1175/JCLI-D-14-00389.1.
- 690 Cavalieri, D., C. Parkinson, P. Gloersen, and H. Zwally, 1996: Sea ice concentrations from nimbus-  
691 7 smmr and dmsp ssm/i-ssmis passive microwave data. *NASA National Snow and Ice Data*  
692 *Center Distributed Active Archive Center*, **41**, doi:10.5067/8GQ8LZQVL0VL.
- 693 Chou, M., and K. Lee, 1996: Parameterizations for the absorption of solar radiation by water vapor  
694 and ozone. *J. Atmos. Sci.*, **53**, 1203–1208.
- 695 Cowtan, K., and R. Way, 2014: Coverage bias in the hadcrut4 temperature series and its impact on  
696 recent temperature trends. *Quart. J. Roy. Meteor. Soc.*, **140** (683), 1935–1944.
- 697 Curry, J., J. Scramm, and E. Ebert, 1994: Sea ice-albedo climate feedback mechanism. *J. Climate*,  
698 **8**, 240–247.

- 699 Ding, Q., A. Schweiger, M. LHeureux, , E. Steig, D. Battisti, and N. Johnson, 2019: Fingerprints  
700 of internal drivers of arctic sea ice loss in observations and model simulations. *Nat. Geo. Sci.*,  
701 **7**, 28–33.
- 702 Ding, Q., and Coauthors, 2017: Influence of high-latitude atmospheric circulation changes on  
703 summertime arctic sea ice. *Nat. Clim. Chang.*, **7**, 289–295.
- 704 Donohoe, A., and D. Battisti, 2011: Atmospheric and surface contributions to planetary albedo. *J.*  
705 *Climate*, **24 (16)**, 4401–4417.
- 706 Donohoe, A., and D. Battisti, 2013: The seasonal cycle of atmospheric heating and temperature.  
707 *J. Climate*, **26 (14)**, 4962–4980.
- 708 Ferreira, D., J. Marshall, and B. Rose, 2011: Climate determinism revisited: multiple equilibria in  
709 a complex climate model. *J. Climate*, **24**, 992–1012.
- 710 Flanner, M., K. Shell, M. Barlage, D. Perovich, and M. Tschudi, 2011: Radiative forcing and  
711 albedo feedback from the northern hemisphere cryosphere between 1979 and 2008. *natgeo*,  
712 **16 (4)**, doi:10.1038/NGEO.
- 713 Flato, G., and Coauthors, 2013: *Evaluation of Climate Models*, book section 8, 659740. Cam-  
714 bridge University Press, doi:10.1017/CBO9781107415324.018.
- 715 Gorodetskaya, I. V., L. Tremblay, B. Liepert, M. A. Cane, and R. Cullather, 2006: The influence  
716 of cloud and surface properties on the arctic shortwave radiation budget in coupled models. *J.*  
717 *Climate*, **21**, 866–883.
- 718 Hall, A., 2004: The role of surface albedo feedback in climate. *J. Climate*, **17**, 1550–1568.

719 Hall, A., and X. Qu, 2006: Using the current seasonal cycle to constrain snow albedo feed-  
720 back in future climate change. *Geophys. Res. Lett.*, **33** (L03502), 1550–1568, doi:10.1029/  
721 2005GL025127.

722 Hansen, J., R. Ruedy, J. Glascoe, and M. Sato, 1999: Giss analysis of surface temperature change.  
723 *J. Geophys. Res.*, **104**, 30 997–31 022.

724 Hansen, J., G. Russell, D. Rind, P. Stone, A. Lacis, S. Lebedeff, R. Ruedy, and L. Travis, 1983:  
725 Efficient three-dimensional global models for climate studies: Models i and ii. *Mon. Weath.*  
726 *Rev.*, **111**, 609–662.

727 Holland, M. M., and C. Bitz, 2003: Polar amplification of climate in coupled models. *Climate*  
728 *Dyn.*, **21**, 221–232.

729 Horvat, C., C. Bitz, and C. Polashenski, 2019: What controls the sea ice albedo feedback? *J.*  
730 *Climate*, **in press**.

731 Hummel, J., and R. Reck, 1979: A global surface albedo model. *J. Adv. Model. Earth Sy.*, **18**,  
732 239–253.

733 Hwang, Y., D. Frierson, and J. Kay, 2011: Coupling between arctic feedbacks and changes in  
734 poleward energy transport. *Geophys. Res. Lett.*, **38**, L17 704, doi:10.1029/2011GL048546.

735 Jones, J., and Coauthors, 2009: Assessing recent trends in high-latitude southern hemisphere  
736 surface climate. *Nat. Clim. Chang.*, **6**, 917–926.

737 Kalnay, E., and Coauthors, 1996: The NCEP/NCAR 40-year reanal-  
738 ysis project. *Bull. Amer. Meteor. Soc.*, URL [https://www.esrl.noaa.](https://www.esrl.noaa.gov/psd/data/gridded/data.ncep.reanalysis.html)  
739 [gov/psd/data/gridded/data.ncep.reanalysis.html](https://www.esrl.noaa.gov/psd/data/gridded/data.ncep.reanalysis.html), [accessed 07-January-2018,  
740 <https://www.esrl.noaa.gov/psd/data/gridded/data.ncep.reanalysis.html>].

741 Kato, S., and Coauthors, 2018: Surface irradiances of edition 4.0 clouds and the Earth's radiant  
742 energy system (CERES) energy balanced and filled (EBAF) data product. *J. Climate*, **31** (11),  
743 4501–4527.

744 Kay, J., M. Holland, C. Bitz, E. Blanchard-Wrigglesworth, A. Gettelman, A. Conley, and D. Bai-  
745 ley, 2012: The influence of local feedbacks and northward heat transport on the equilibrium  
746 arctic climate response to increased greenhouse gas forcing. *J. Climate*, **25**, 5433–5450.

747 Kay, J., M. Holland, and A. Jahn, 2011: Inter-annual to multi-decadal arctic sea ice extent trends  
748 in a warming world. *Geophys. Res. Lett.*, **38** (L08503), doi:10.1029/2011GL048008.

749 Lindsay, R., M. Wensnaham, A. Schweiger, and J. Zhang, 2014: Evaluation of seven different  
750 atmospheric reanalysis products in the arctic. *J. Climate*, **27**, 2588–2606.

751 Loeb, N. G., and Coauthors, 2018: Clouds and the Earth's radiant energy system (CERES) en-  
752 ergy balanced and filled (EBAF) top-of-atmosphere (TOA) edition 4.0 data product. *J. Climate*,  
753 **31** (2), 895–918.

754 Mahlstein, I., and R. Knutti, 2012: September arctic sea ice predicted to disappear near 2 degrees  
755 c global warming above present. *J. Geophys. Res.*, **117** (D06104).

756 Meehl, G. A., C. Covey, T. Delworth, M. Latif, B. McAvaney, J. F. B. Mitchell, R. J. Stouffer,  
757 and K. E. Taylor, 2007: The WCRP CMIP3 multi-model dataset: A new era in climate change  
758 research. *Bull. Amer. Meteor. Soc.*, **88**, 1383–1394.

759 Morice, C. P., J. Kennedy, N. Rayner, and P. Jones, 2012: Quantifying uncertainties in global  
760 and regional temperature change using an ensemble of observational estimates: The hadcrut4  
761 dataset. *J. Geophys. Res.*, **117**, D08 101.

- 762 North, G. R., 1984: The small ice cap instability in diffusive climate models. *J. Atmos. Sci.*,  
763 **41 (23)**, 3390–3395.
- 764 Pendergrass, A. C., A. G., and F. Vitt, 2018: Surface and top-of-atmosphere radiative feedback  
765 kernels for cesm-cam5. *Earth Sys. Sci. Data*, **10**, 317–324.
- 766 Perovich, D., T. Grenfell, B. Light, and P. Hobbs, 2002: Seasonal evolution of the albedo of  
767 multiyear arctic sea ice. *J. Geophys. Res.*, doi:10.1029/2000JC000438.
- 768 Pistone, K., I. Eisenman, and V. Ramanathan, 2014: Observational determination of albedo de-  
769 crease caused by vanishing arctic sea ice. *Proc. Natl. Acad. Sci.*, **111 (9)**, 3322–3326.
- 770 Pistone, K., I. Eisenman, and V. Ramanathan, 2019: Radiative heating of an ice-free arctic ocean.  
771 *Geophys. Res. Lett.*, **46 (13)**, 7474–7480.
- 772 Polvani, L., and K. Smith, 2013: Can natural variability explain the observed antarctic sea ice  
773 trends? New modeling evidence from CMIP5. *Geophys. Res. Lett.*, **40 (2)**, 3195–3199.
- 774 Previdi, M., 2010: Radiative feedbacks on global precipitation. *Environ. Res. Lett.*, **5**, doi:doi:  
775 10.1088/1748-9326/5/2/025211.
- 776 Qu, X., and A. Hall, 2005: Surface contribution to planetary albedo variability in the cryosphere  
777 regions. *J. Climate*, **18**, 5239–5252.
- 778 Roe, G., 2009: Feedbacks, timescales, and seeing red. *Annu. Rev. Earth Planet. Sci.*, **37**, 930–115.
- 779 Rosenblum, E., and I. Eisenman, 2016: Faster arctic sea ice retreat in cmip5 than in cmip3 due to  
780 volcanoes. *J. Climate*, **29**, 9179–9188.
- 781 Schneider, A., M. Flanner, and J. Perket, 2018: Multidecadal variability in surface albedo feedback  
782 across cmip5 models. *grl*, doi:10.1002/2017GL076293.

783 Shell, K., J. Kiehl, and C. Shields, 2008: Using the radiative kernel technique to calculate climate  
784 feedbacks in ncar's community atmospheric model. *J. Climate*, **21**, 2269–2282.

785 Shu, Q., Z. Song, and F. Qiao, 2015: Assessment of sea ice simulations in the cmip5 models.  
786 *Cryosphere*, **9**, 399–409.

787 Sledd, A., and T. L'Ecuyer, 2019: How much do clouds mask the impact of arctic sea ice and snow  
788 cover variations? different perspectives from observations and reanalyses. *Atmosphere*, **10** (1),  
789 doi:10.3390/atmos10010012.

790 Smith, C., and Coauthors, 2018: Understanding rapid adjustments to diverse forcing agents.  
791 *Geophys. Res. Lett.*, doi:10.1029/2018GL079826.

792 Soden, B., and I. Held, 2006a: An assessment of climate feedbacks in coupled oceanatmosphere  
793 models. *J. Climate*, **19**, 3354–3360.

794 Soden, B., and I. Held, 2006b: An assessment of climate feedbacks in coupled oceanatmosphere  
795 models. *J. Climate*, **19**, 3354–3360.

796 Stocker, T., and Coauthors, 2013: *Technical Summary*, book section TS, 33115. Cambridge  
797 University Press, Cambridge, United Kingdom and New York, NY, USA, doi:10.1017/  
798 CBO9781107415324.005.

799 Stroeve, J., and D. Notz, 2015: Insights on past and future sea-ice evolution from combining  
800 observations and models. *Global Planet. Change*, **135**, 119–132.

801 Taylor, K., M. Crucifix, P. Braconnot, C. Hewitt, C. Doutriaux, A. Broccoli, J. Mitchell, and  
802 M. Webb, 2007: Estimating shortwave radiative forcing and response in climate models. *J.*  
803 *Climate*, **20**, 2530–2543.

- 804 Taylor, K., R. Stouffer, and G. Meehl, 2012: An overview of cmip5 and the experiment design.  
805 *Bull. Amer. Meteor. Soc.*, **93**, 485–498.
- 806 Trenberth, K. E., and J. T. Fasullo, 2010: Simulation of present day and 21st century energy  
807 budgets of the southern oceans. *J. Climate*, **23**, 440–454.
- 808 Vavrus, S., D. Waliser, A. Schweiger, and J. Francis, 2009: Simulations of 20th and 21st century  
809 arctic cloud amount in the global climate models assessed in the ipcc ar4. *Climate Dyn.*, **33** (7),  
810 1099–1115.
- 811 Wang, X., and J. Key, 2005: Arctic surface, cloud, and radiation properties based on the avhrr  
812 polar pathfinder dataset. part i: Spatial and temporal characteristics. *J. Climate*, **18**, 2558–2574.
- 813 Yu, L., R. Weller, and B. Sun, 2006: Surface albedo feedback estimates from the AR4 climate  
814 models. *J. Climate*, **19**, 359–365.

815 **LIST OF TABLES**

816 **Table 1.** SIAF values (in  $W m^{-2} K^{-1}$ ) for the (top) Arctic and (bottom) Southern Ocean  
 817 derived from (left) Observations and model simulations of (middle) 4XCO<sub>2</sub>  
 818 and (right) historical simulations. Each value shows the central estimate and  
 819  $2\sigma$  range across the bootstrapping Monte-Carlo simulations for the observa-  
 820 tions and inter-model spread for the models. The top row in each hemisphere  
 821 shows the full calculation using the model specific RS and IS. The second row  
 822 shows the impact of inter-model differences in IS as calculated using the model  
 823 specific IS and the observed RS. The third row shows the impact of inter-model  
 824 differences in RS as calculated using the model specific RS and the observed IS. . . . 39

825 **Table 2.** Ice albedo feedback in CMIP5 climate models calculated using the methodol-  
 826 ogy of this study – with a model specific RS from the isotropic model– com-  
 827 pared to that calculated using RS from the GFDL surface albedo kernel for all  
 828 models. The CMIP5 ensemble mean and  $2\sigma$  are shown for each hemisphere  
 829 and divided into ocean and full domains. . . . . 40

TABLE 1: SIAF values (in  $\text{W m}^{-2} \text{K}^{-1}$ ) for the (top) Arctic and (bottom) Southern Ocean derived from (left) Observations and model simulations of (middle) 4XCO<sub>2</sub> and (right) historical simulations. Each value shows the central estimate and  $2\sigma$  range across the bootstrapping Monte-Carlo simulations for the observations and inter-model spread for the models. The top row in each hemisphere shows the full calculation using the model specific RS and IS. The second row shows the impact of inter-model differences in IS as calculated using the model specific IS and the observed RS. The third row shows the impact of inter-model differences in RS as calculated using the model specific RS and the observed IS.

<b>Arctic</b>			
	Observations	4XCO <sub>2</sub>	Historical
Full Calculation	$0.16 \pm 0.04$	$0.13 \pm 0.09$	$0.12 \pm 0.13$
IS contribution $RS_{OBS} \times IS$		$0.13 \pm 0.08$	$0.12 \pm 0.12$
RS contribution $RS \times IS_{OBS}$		$0.16 \pm 0.04$	$0.16 \pm 0.04$
<b>Southern Ocean</b>			
	Observations	4XCO <sub>2</sub>	Historical
Full Calculation		$0.08 \pm 0.13$	
IS contribution $RS_{OBS} \times IS$		$0.07 \pm 0.11$	
RS contribution $RS \times IS_{OBS}$		$0.08 \pm 0.04$	

TABLE 2: Ice albedo feedback in CMIP5 climate models calculated using the methodology of this study – with a model specific RS from the isotropic model– compared to that calculated using RS from the GFDL surface albedo kernel for all models. The CMIP5 ensemble mean and  $2\sigma$  are shown for each hemisphere and divided into ocean and full domains.

<b>Northern Hemisphere</b>		
	Ocean Domain	Total
This Study	$0.15 \pm .10$	$0.27 \pm 0.18$
GFDL RS kernel	$0.11 \pm 0.06$	$0.20 \pm 0.11$
<b>Southern Hemisphere</b>		
	Ocean Domain	Total
This Study	$0.09 \pm 0.16$	$0.10 \pm 0.17$
GFDL RS kernel	$0.08 \pm 0.14$	$0.09 \pm 0.15$
<b>Global</b>		
	Ocean Domain	Total
This Study	$0.24 \pm 0.15$	$0.37 \pm 0.19$
GFDL RS kernel	$0.19 \pm 0.11$	$0.29 \pm 0.13$

830 **LIST OF FIGURES**

831 **Fig. 1.** Arctic summertime (MJJA) surface albedo radiative sensitivity (RS) calculated from radia-  
832 tive kernels (upper panels) and estimated from the climatological radiative fields using the  
833 idealized isotropic radiation model (lower panels) in the same models. The squared spatial  
834 correlation coefficient between the kernel isotropic methods in the same model are provided  
835 in the middle and the Arctic domain averaged values are shown in the upper right of each  
836 panel. Note that there is no RS calculation from the GFDL model because mean state fields  
837 from this simulation were not saved. . . . . 44

838 **Fig. 2.** As in Fig. 1 but for the NDJF RS in the Southern Ocean. Domain averaged surface albedo  
839 feedbacks exclude the Antarctic continent. Note that the figures are ordered by domain  
840 average RS over the Southern Ocean and this order differs from Fig. 1. . . . . 45

841 **Fig. 3.** Schematic of the single layer isotropic model modified from T07. . . . . 46

842 **Fig. 4.** Comparison of Arctic Summertime (MJJA) full sky and clear sky surface albedo kernels. . . . 47

843 **Fig. 5.** Comparison of the atmospheric opacity parameters that result from the application of the  
844 isotropic model to the Arctic summertime (MJJA) mean state radiative fields in the different  
845 climate models and observations. (Top Row) All-sky RS repeated from Fig. 1. (Second  
846 Row) Cloud reflectivity defined as the isotropic reflectivity applied to the all-sky radiative  
847 fields minus that defined from the clear-sky fields with the latter shown in the third row.  
848 (Bottom row) All-sky absorptivity. The (full Arctic) domain average is shown in the upper  
849 right of each panel. The four models for which kernels are available are shown to the left  
850 columns and the observational calculation from CERES data is shown to the right. . . . . 48

851 **Fig. 6.** Arctic summertime (MJJA) radiative sensitivity estimated using the isotropic model and the  
852 climatological radiation fields for CMIP5 historical simulations. Models are ordered as in  
853 reading a book (left to right then down) according to the domain average albedo feedback.  
854 Asterisks denote the models for which radiative kernel calculations are available that have  
855 been repeated from Fig. 1. The dark purple line shows the sea ice edge designated by the  
856 MJJA 50 % sea ice concentration contour. The full domain spatial average is shown in the  
857 upper left corner of each panel in black, the Arctic ocean average is shown in the lower right  
858 corner in blue and, the spatial average over the sea ice is shown in the lower left corner in  
859 purple. Observational estimates from CERES satellite data are shown in the bottom right  
860 panel. . . . . 49

861 **Fig. 7.** As in Fig. 6 but for the NDJF Southern Ocean RS. Domain averaged surface albedo feed-  
862 backs exclude the Antarctic continent. The dark purple line shows the sea ice edge desig-  
863 nated by the NDJF 50 % sea ice concentration contour. Note that models are ordered by  
864 Southern Ocean domain averaged RS and this order differs from that in Fig. 6. Asterisks de-  
865 note the models for which radiative kernel calculations are available that have been repeated  
866 from Fig. 2. . . . . 50

867 **Fig. 8.** Spatial maps of observational estimates of summertime (MJJA) radiative sensitivity(RS,  
868 top), ice sensitivity (IS, middle) and the radiative impact of surface albedo change ( $RI_{TOA,\alpha}$ ,  
869 bottom). The RS is calculated from the isotropic shortwave model applied to the CERES  
870 data. The IS is calculated from Observational Best Estimate (OBE) surface albedo change  
871 between 1982 and 2016 divided by the global mean surface temperature change. The left  
872 panels show the central estimates of each quantity and the right panels show the uncertainty  
873 (2 standard deviations,  $\sigma$ ) calculated from a Monte Carlo bootstrapping re-sampling with  
874 replacement as described in the Appendix. . . . . 51

875 **Fig. 9.** Estimates of global (and annual) SIAF from climate models and observations using the ra-  
 876 diative sensitivity (RS) from the isotropic model applied to the climatology and the change  
 877 in surface albedo under external forcing normalized by the global mean temperature change.  
 878 (Upper left) Arctic sea ice changes over the historical (2007 to 2016 minus 1982 to 1991 av-  
 879 erages). The black bars show the CMIP5 model distribution using the climate model specific  
 880 radiative sensitivity and ice changes, the blue bars show the distribution using the model spe-  
 881 cific sea ice changes and observational RS and the red bars show the distribution using the  
 882 observational sea ice change and model specific radiative sensitivity. Solid vertical lines  
 883 show the model mean of each distribution. The dashed vertical line shows the observational  
 884 estimate. The overlaid dark and thinner distribution shows the histogram of observational  
 885 estimates of ice albedo feedback calculated from a Monte Carlo re-sampling of subsets of  
 886 the ice albedo data and radiative data; the black distribution shows the impact of uncer-  
 887 tainties in the observational RS and IS combined, the blue distribution shows the impact of  
 888 the IS uncertainty only and the red shows the impact of the RS uncertainty only. (Lower  
 889 Left) As in the above panel except using the modeled changes in the 4XCO<sub>2</sub> simulations.  
 890 (Lower Right) Distribution of surface albedo feedback in the Southern Ocean diagnosed  
 891 from 4XCO<sub>2</sub> normalized sea ice changes. Because the observational estimate of sea ice  
 892 changes over the historical simulation is not statistically significant, the red distribution is  
 893 calculated from the model specific radiative sensitivity and the model mean normalized sea  
 894 ice change. . . . . 52

895 **Fig. 10.** Comparison of ice albedo feedback calculated from CMIP5 4XCO<sub>2</sub> using (ordinate) the  
 896 method of Soden and Held (2006b) with RS in all models set to the GFDL surface albedo  
 897 kernel versus (abscissa) the method introduced here with RS calculated from the model  
 898 specific climatological radiative fluxes via the isotropic model. The blue markers show the  
 899 contribution of the ocean domain only and the red markers show the full domain. All values  
 900 shown are the contribution to the global mean. Dots show individual models and filled  
 901 squares show the ensemble average with bars showing one standard deviation of the mean.  
 902 The upper left shows the NH, the upper right the SH and the bottom the global mean. The  
 903 black line is the 1:1 line. . . . . 53

904 **Fig. A1.** Arctic summertime (MJJA) surface albedo radiative sensitivity (RS) calculated from radia-  
 905 tive kernels (upper panels) and estimated from the climatological radiative fields using the  
 906 idealized isotropic radiation model of T07 (middle panels) and (Donohoe and Battisti 2011)  
 907 in the same models (bottom panels). The squared spatial correlation coefficient between  
 908 the kernel isotropic methods in the same model are provided in the middle and the Arctic  
 909 domain averaged values are shown in the upper right of each panel. . . . . 54

910 **Fig. A2.** (Top panel) Scatter plot of MJJA radiative sensitivity calculated by (ordinate) radiative ker-  
 911 nels and (abscissa) the isotropic model from the mean state in the same climate model. All  
 912 four climate models and Arctic gridpoints considered collectively. (Bottom panel) Scat-  
 913 ter plot of MJJA radiative sensitivity calculated from radiative kernels in one model versus  
 914 the radiative sensitivity calculated from radiative kernels in a different model (selected at  
 915 random). The dashed black line shows the 1:1 line. . . . . 55

916 **Fig. A3.** (Top panel) Scatter plot of NDJFM radiative sensitivity calculated by (ordinate) radiative  
 917 kernels and (abscissa) the isotropic model from the mean state in the same climate model.  
 918 All four climate models and Southern Ocean gridpoints considered collectively. (Bottom  
 919 panel) Scatter plot of NDJF radiative sensitivity calculated from radiative kernels in one  
 920 model versus the radiative sensitivity calculated from radiative kernels in a different model  
 921 (selected at random). The dashed black line shows the 1:1 line. . . . . 56

922 **Fig. A4.** Comparison of the (MJJA) surface albedo changes (1982-2016) calculated from the NSIDC  
923 sea ice concentration data (left) and the APP-X surface albedo data (right). . . . . 57

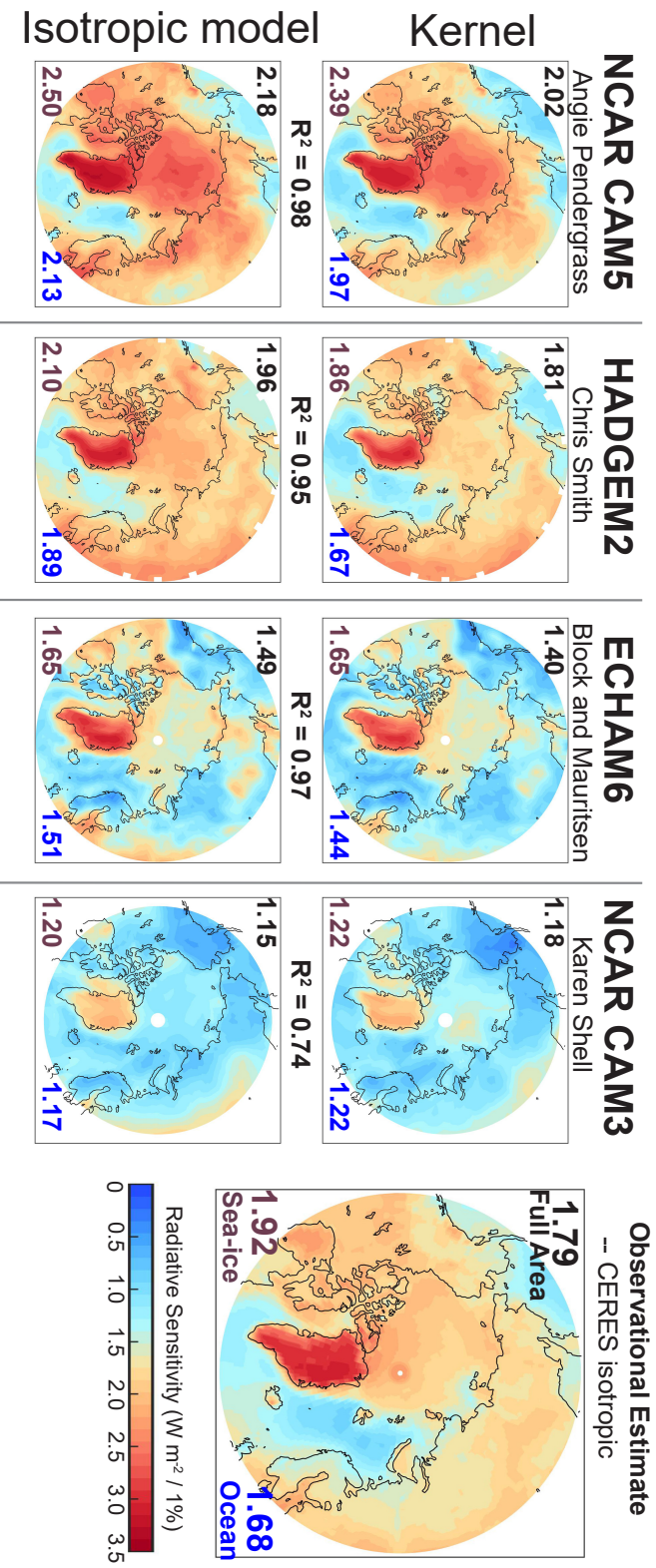


FIG. 1: Arctic summertime (MJA) surface albedo radiative sensitivity (RS) calculated from radiative kernels (upper panels) and estimated from the climatological radiative fields using the idealized isotropic radiation model (lower panels) in the same models. The squared spatial correlation coefficient between the kernel isotropic methods in the same model are provided in the middle and the Arctic domain averaged values are shown in the upper right of each panel. Note that there is no RS calculation from the GFDL model because mean state fields from this simulation were not saved.

Observational estimates from CERES EBAF satellite data and the isotropic model are shown to the right.

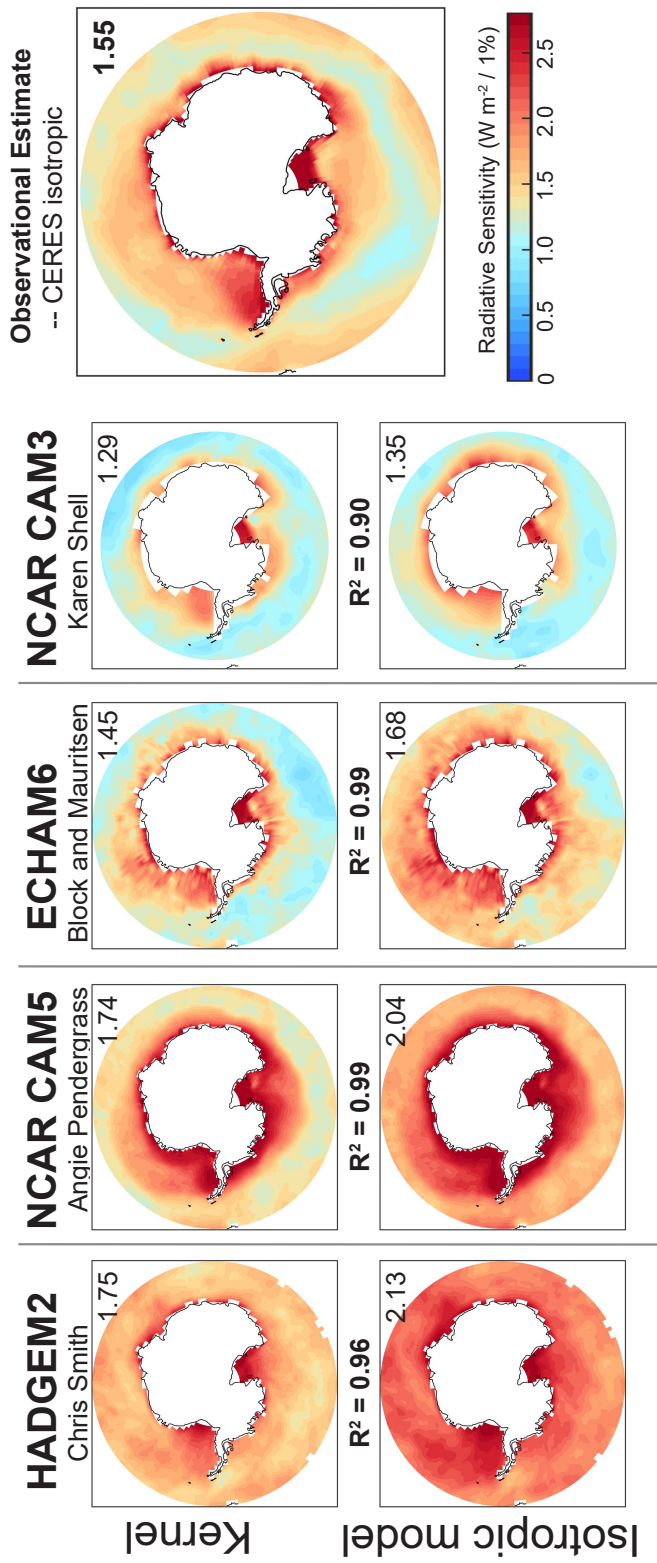


FIG. 2: As in Fig. 1 but for the NDJF RS in the Southern Ocean. Domain averaged surface albedo feedbacks exclude the Antarctic continent. Note that the figures are ordered by domain average RS over the Southern Ocean and this order differs from Fig. 1.

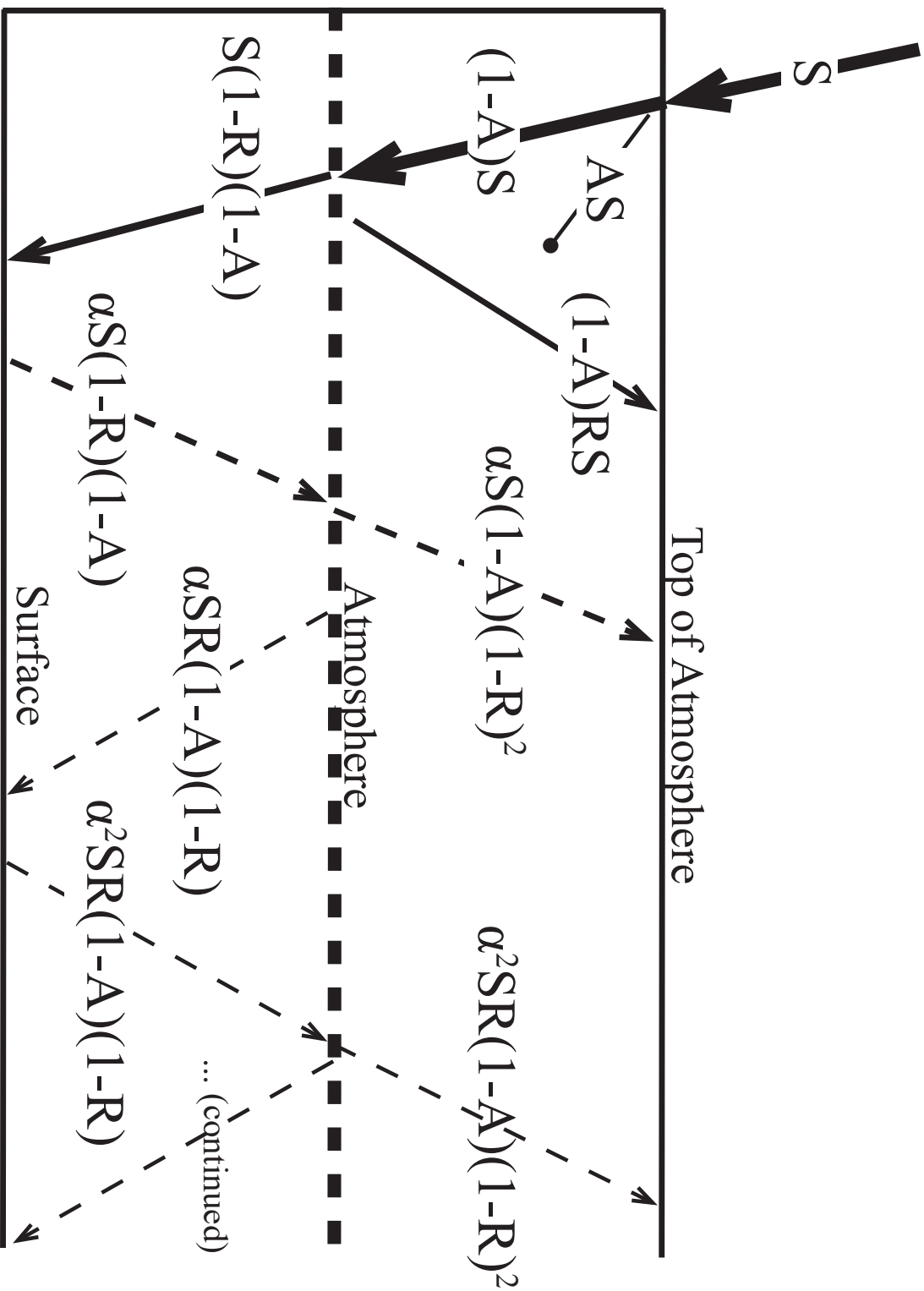


FIG. 3: Schematic of the single layer isotropic model modified from T07.

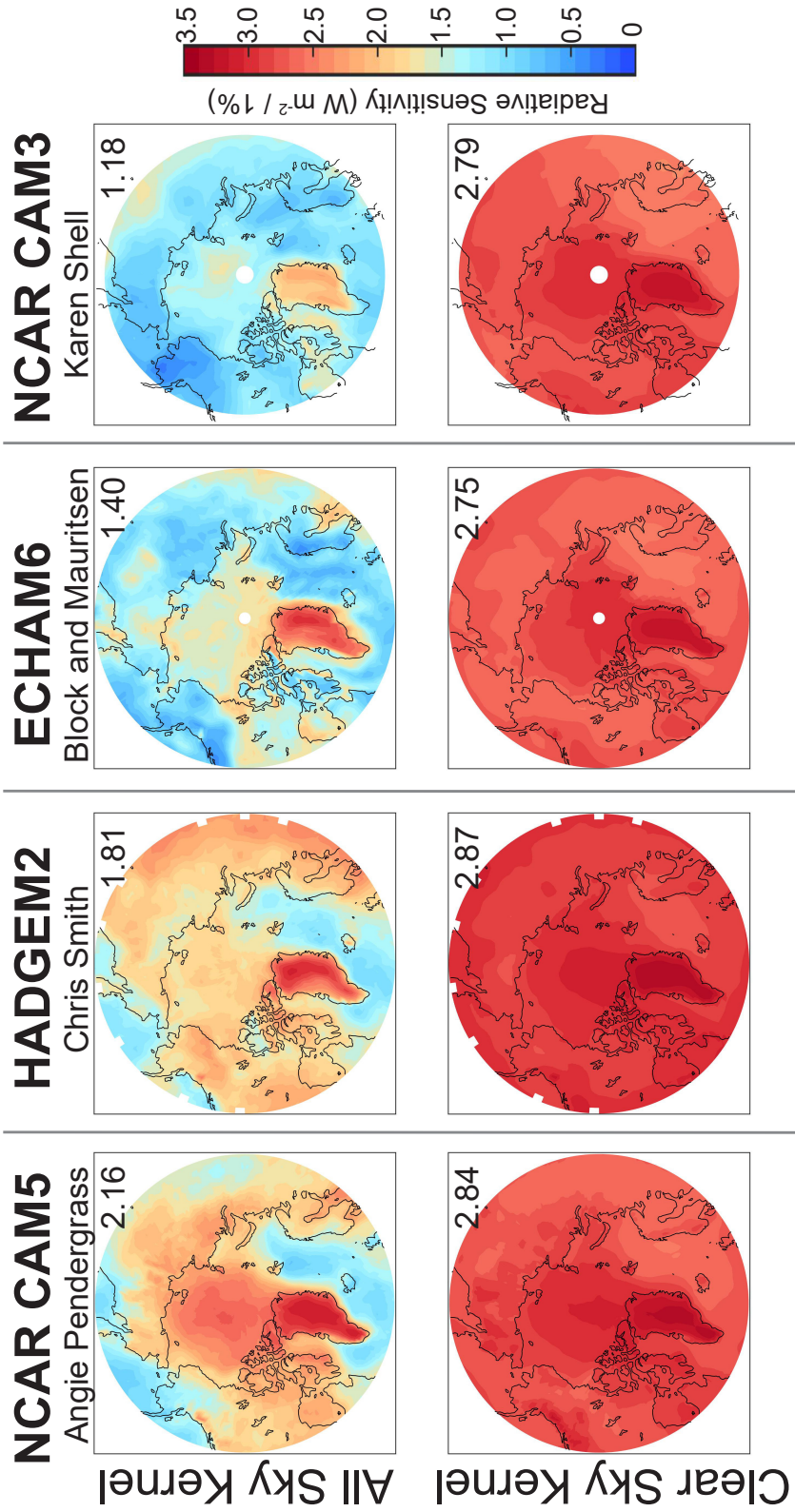


FIG. 4: Comparison of Arctic Summertime (MJJJA) full sky and clear sky surface albedo kernels.

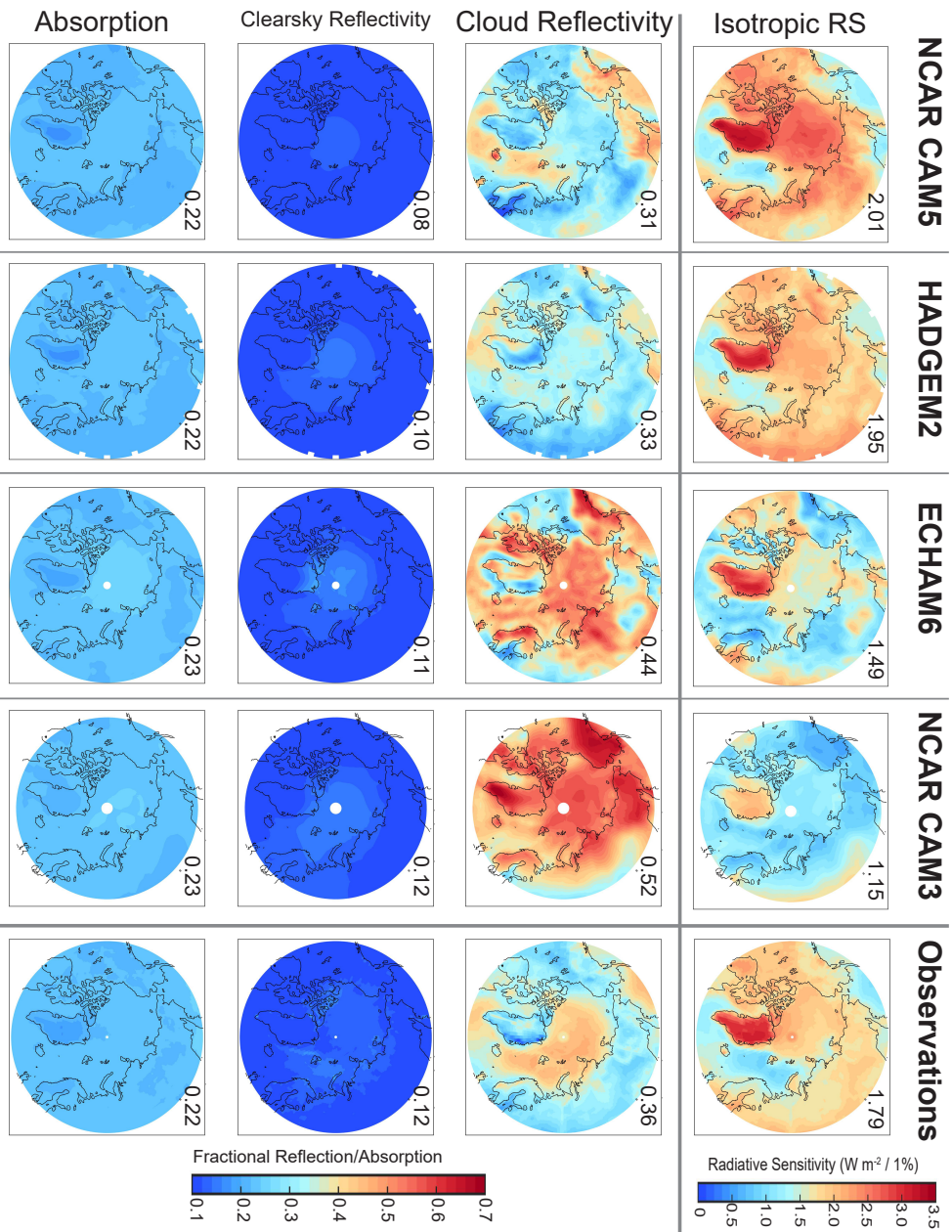


FIG. 5: Comparison of the atmospheric opacity parameters that result from the application of the isotropic model to the Arctic summertime (MJJJA) mean state radiative fields in the different climate models and observations. (Top Row) All-sky RS repeated from Fig. 1. (Second Row) Cloud reflectivity defined as the isotropic reflectivity applied to the all-sky radiative fields minus that defined from the clear-sky fields with the latter shown in the third row. (Bottom row) All-sky absorptivity. The (full Arctic) domain average is shown in the upper right of each panel. The four models for which kernels are available are shown to the left columns and the observational calculation from CERES data is shown to the right.



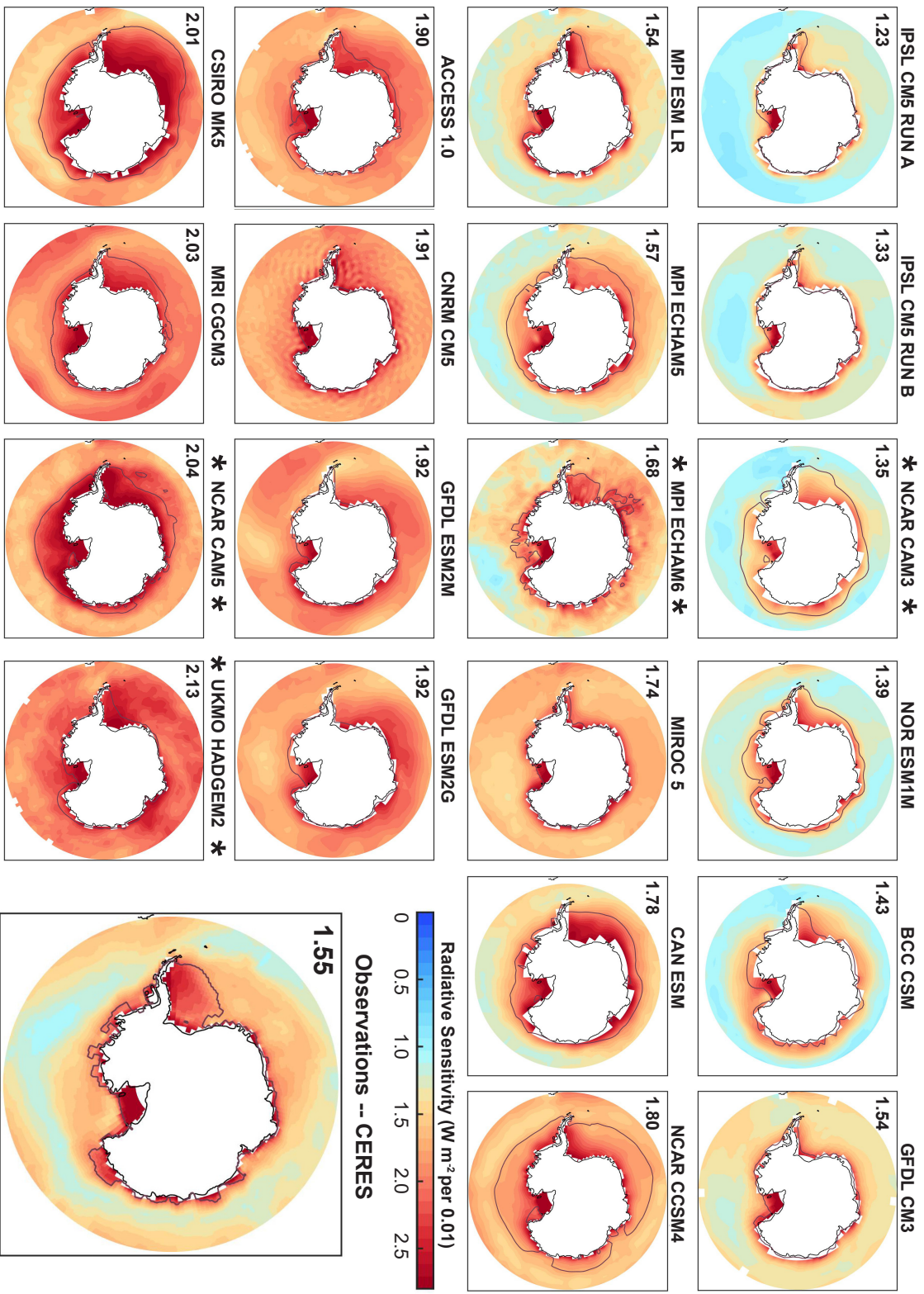


FIG. 7: As in Fig. 6 but for the NDJF Southern Ocean RS. Domain averaged surface albedo feedbacks exclude the Antarctic continent. The dark purple line shows the sea ice edge designated by the NDJF 50 % sea ice concentration contour. Note that models are ordered by Southern Ocean domain averaged RS and this order differs from that in Fig. 6. Asterisks denote the models for which radiative kernel calculations are available that have been repeated from Fig. 2.

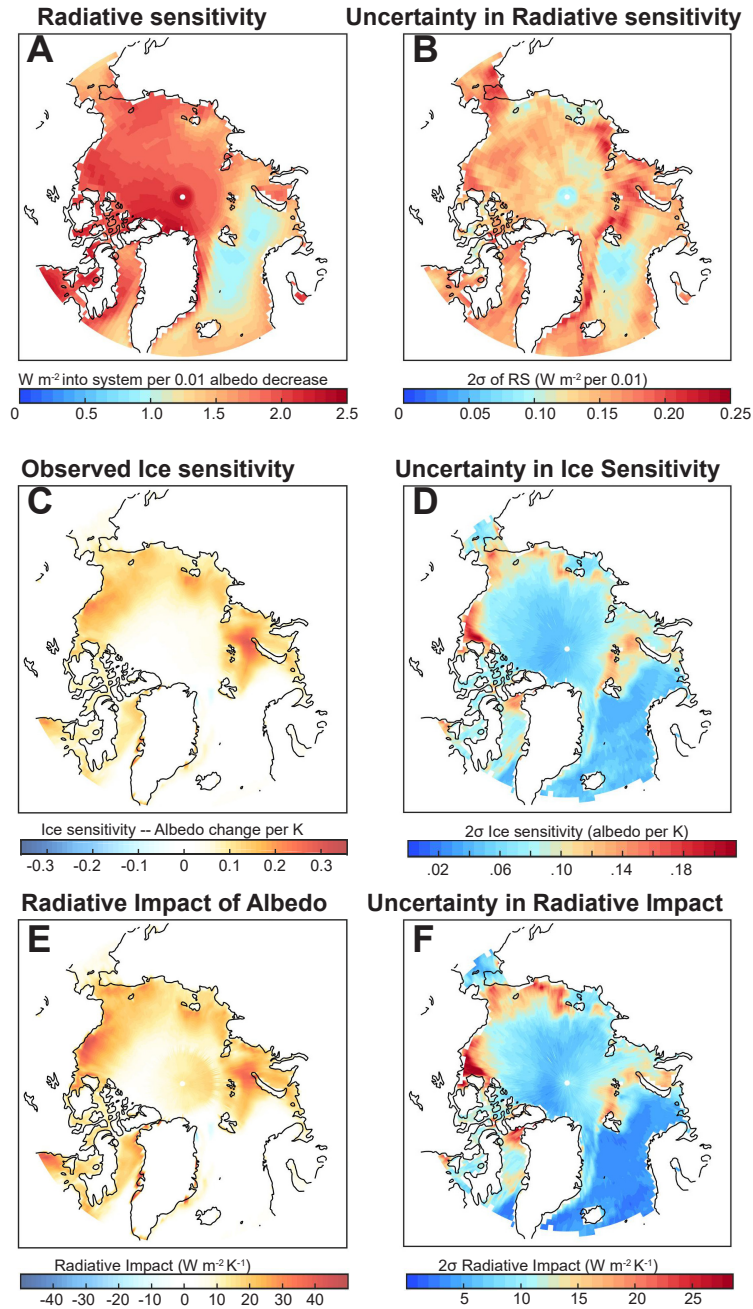
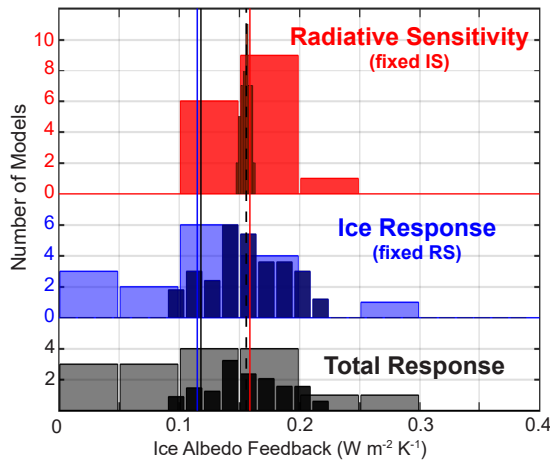
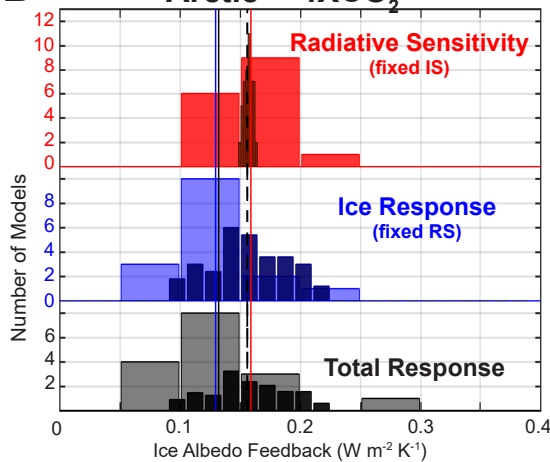


FIG. 8: Spatial maps of observational estimates of summertime (MJJA) radiative sensitivity (RS, top), ice sensitivity (IS, middle) and the radiative impact of surface albedo change ( $RI_{T_{OA},\alpha}$ , bottom). The RS is calculated from the isotropic shortwave model applied to the CERES data. The IS is calculated from Observational Best Estimate (OBE) surface albedo change between 1982 and 2016 divided by the global mean surface temperature change. The left panels show the central estimates of each quantity and the right panels show the uncertainty (2 standard deviations,  $\sigma$ ) calculated from a Monte Carlo bootstrapping re-sampling with replacement as described in the Appendix.

## A Arctic -- Historical Simulation



## B Arctic -- 4XCO<sub>2</sub>



## C Southern Ocean -- 4XCO<sub>2</sub>

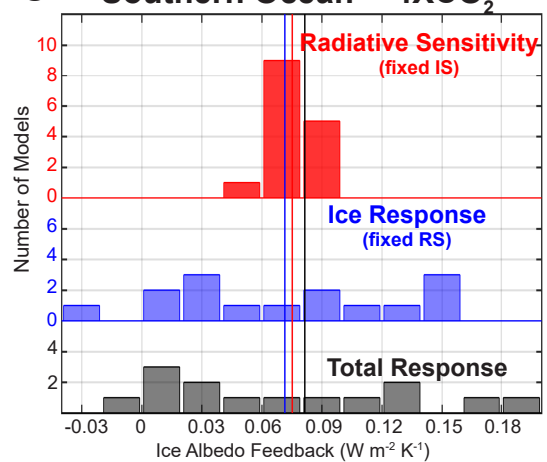


FIG. 9: Estimates of global (and annual) SIAF from climate models and observations using the radiative sensitivity (RS) from the isotropic model applied to the climatology and the change in surface albedo under external forcing normalized by the global mean temperature change. (Upper left) Arctic sea ice changes over the historical (2007 to 2016 minus 1982 to 1991 averages). The black bars show the CMIP5 model distribution using the climate model specific radiative sensitivity and ice changes, the blue bars show the distribution using the model specific sea ice changes and observational RS and the red bars show the distribution using the observational sea ice change and model specific radiative sensitivity. Solid vertical lines show the model mean of each distribution. The dashed vertical line shows the observational estimate. The overlaid dark and thinner distribution shows the histogram of observational estimates of ice albedo feedback calculated from a Monte Carlo re-sampling of subsets of the ice albedo data and radiative data; the black distribution shows the impact of uncertainties in the observational RS and IS combined, the blue distribution shows the impact of the IS uncertainty only and the red shows the impact of the RS uncertainty only. (Lower Left) As in the above panel except using the modeled changes in the 4XCO<sub>2</sub> simulations. (Lower Right) Distribution of surface albedo feedback in the Southern Ocean diagnosed from 4XCO<sub>2</sub> normalized sea ice changes. Because the observational estimate of sea ice changes over the historical simulation is not statistically significant, the red distribution is calculated from the model specific radiative sensitivity and the model mean normalized sea ice change.

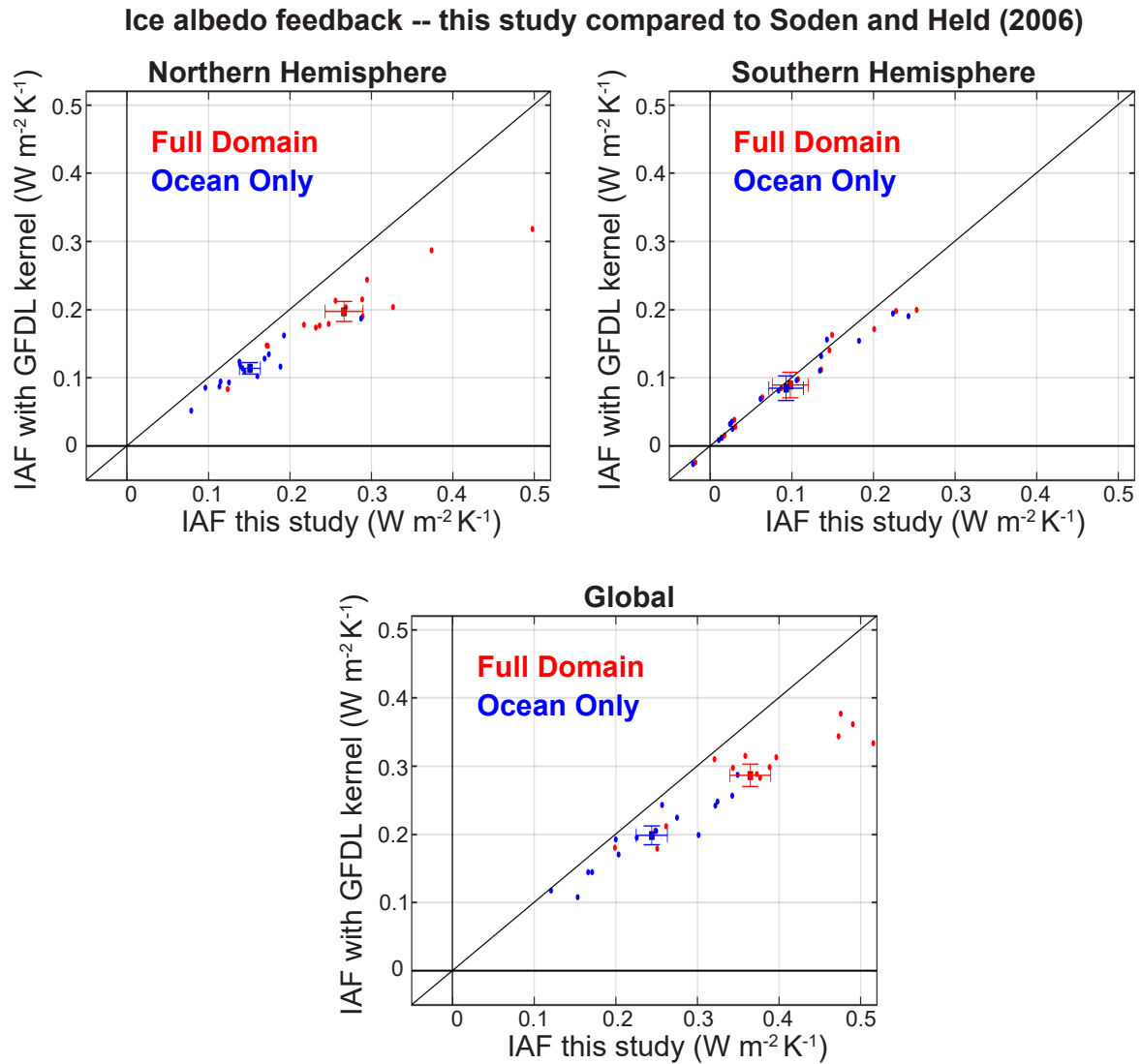


FIG. 10: Comparison of ice albedo feedback calculated from CMIP5 4XCO<sub>2</sub> using (ordinate) the method of Soden and Held (2006b) with RS in all models set to the GFDL surface albedo kernel versus (abscissa) the method introduced here with RS calculated from the model specific climatological radiative fluxes via the isotropic model. The blue markers show the contribution of the ocean domain only and the red markers show the full domain. All values shown are the contribution to the global mean. Dots show individual models and filled squares show the ensemble average with bars showing one standard deviation of the mean. The upper left shows the NH, the upper right the SH and the bottom the global mean. The black line is the 1:1 line.

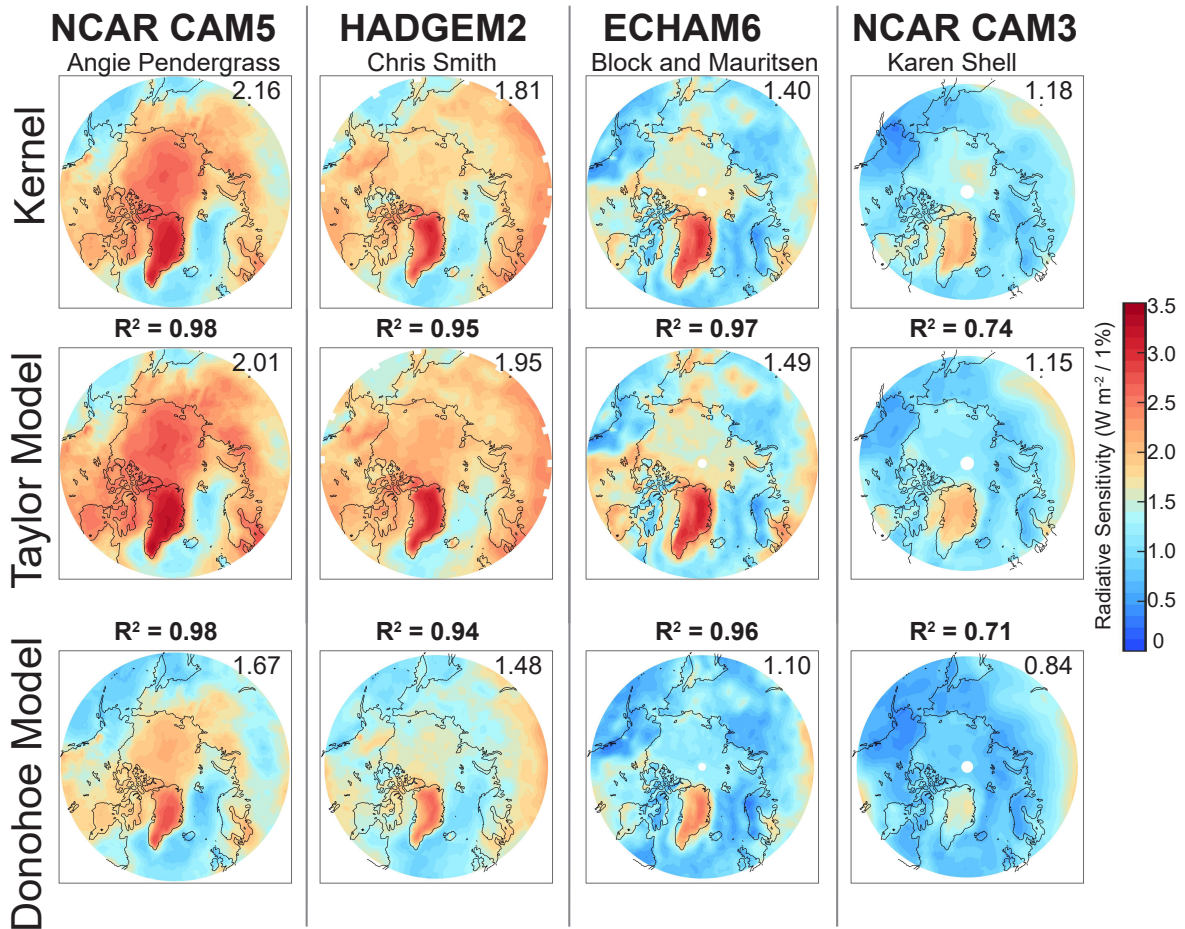


Fig. A1: Arctic summertime (MJJA) surface albedo radiative sensitivity (RS) calculated from radiative kernels (upper panels) and estimated from the climatological radiative fields using the idealized isotropic radiation model of T07 (middle panels) and (Donohoe and Battisti 2011) in the same models (bottom panels). The squared spatial correlation coefficient between the kernel isotropic methods in the same model are provided in the middle and the Arctic domain averaged values are shown in the upper right of each panel.

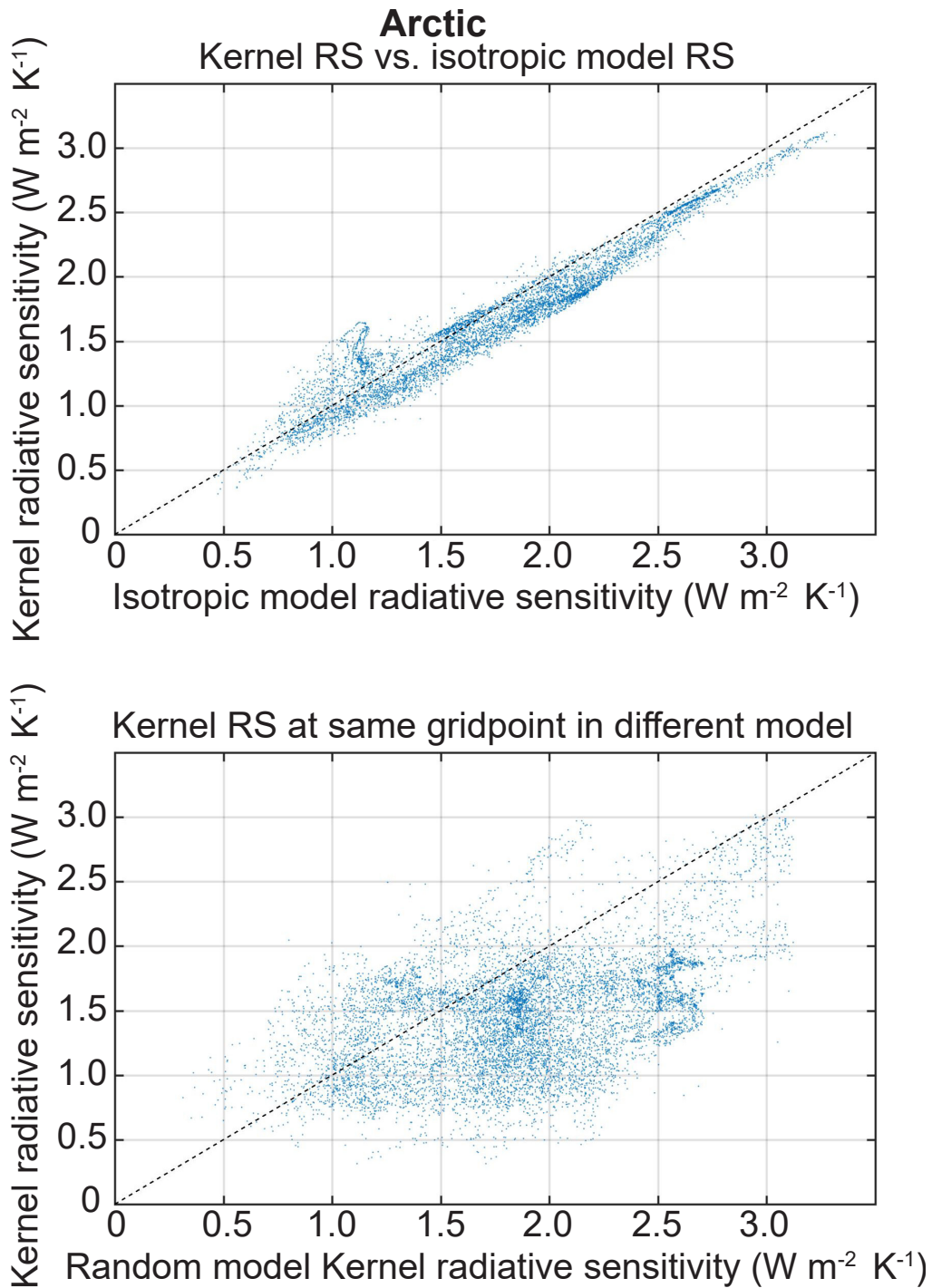


Fig. A2: (Top panel) Scatter plot of MJJA radiative sensitivity calculated by (ordinate) radiative kernels and (abscissa) the isotropic model from the mean state in the same climate model. All four climate models and Arctic gridpoints considered collectively. (Bottom panel) Scatter plot of MJJA radiative sensitivity calculated from radiative kernels in one model versus the radiative sensitivity calculated from radiative kernels in a different model (selected at random). The dashed black line shows the 1:1 line.

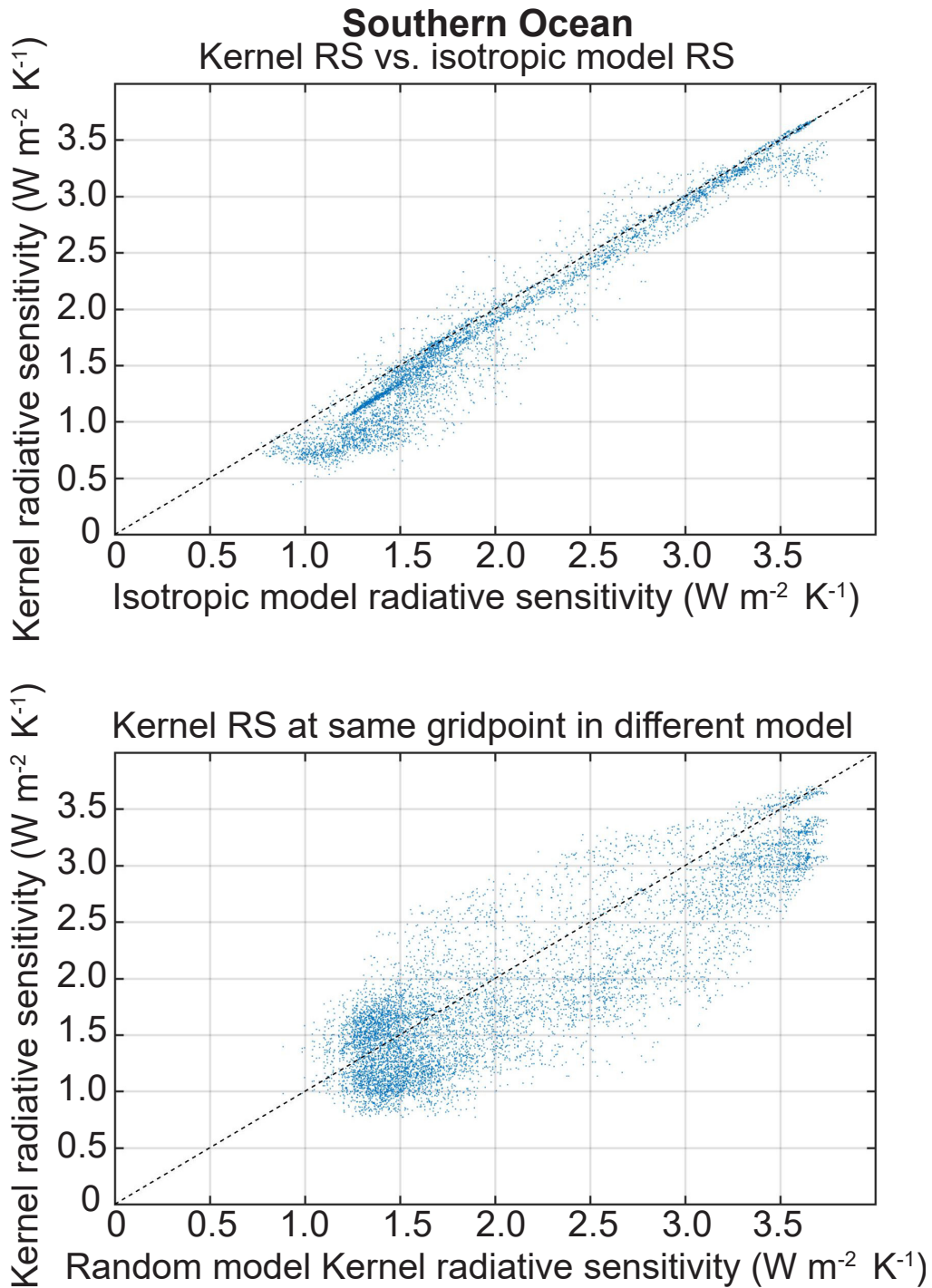


Fig. A3: (Top panel) Scatter plot of NDJFM radiative sensitivity calculated by (ordinate) radiative kernels and (abscissa) the isotropic model from the mean state in the same climate model. All four climate models and Southern Ocean gridpoints considered collectively. (Bottom panel) Scatter plot of NDJF radiative sensitivity calculated from radiative kernels in one model versus the radiative sensitivity calculated from radiative kernels in a different model (selected at random). The dashed black line shows the 1:1 line.

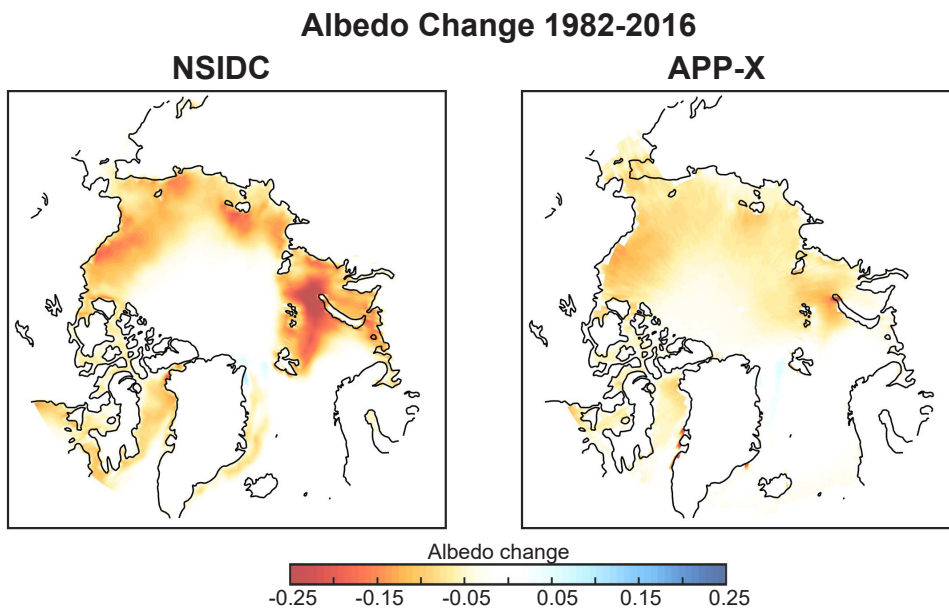


Fig. A4: Comparison of the (MJJA) surface albedo changes (1982-2016) calculated from the NSIDC sea ice concentration data (left) and the APP-X surface albedo data (right).